Blast Overpressure Relief Using Air Vacated Buffer Medium

by

Srikanti Rupa Avasarala

B.Tech., Mechanical Engineering
Indian Institute of Technology, Madras (2007)

Submitted to the School of Engineering
in Partial Fulfillment of the Requirements for the Degree of
Master of Science in Computation for Design and Optimization at the

MASSACHUSETTS INSTITUTE OF TECHNOLOGY

June 2009

Author .....
School of Engineering
May 8, 2009

Certified by .....
Raúl A. Radovitzky
Associate Professor, Aeronautics and Astronautics
Thesis Supervisor

Accepted by .....
Jaime Peraire
Professor of Aeronautics and Astronautics
Director, Computation for Design and Optimization Program

Blast Overpressure Relief Using Air Vacated Buffer Medium

by

Srikanti Rupa Avasarala

Submitted to the School of Engineering
on May 8, 2009, in partial fulfillment of the
requirements for the degree of
Master of Science in Computation for Design and Optimization

Abstract

Blast waves generated by intense explosions cause damage to structures and human injury. In this thesis, a strategy is investigated for relief of blast overpressure resulting from explosions in air. The strategy is based on incorporating a layer of low pressure-low density air in between the blast wave and the target structure. Simulations of blast waves interacting with this air-vacated layer prior to arrival at a fixed wall are conducted using a Computational Fluid Dynamics (CFD) framework. Pressure histories on the wall are recorded from the simulations and used to investigate the potential benefits of vacated air layers in mitigating blast metrics such as peak reflected pressure from the wall and maximum transmitted impulse to the wall. It is observed that these metrics can be reduced by a significant amount by introducing the air-vacated buffer especially for incident overpressures of the order of a few atmospheres. This range of overpressures could be fatal to the human body which makes the concept very relevant for mitigation of human blast injuries. We establish a functional dependence of the mitigation metrics on the blast intensity, the buffer pressure and the buffer length.

In addition, Riemann solutions are utilized to analyze the wave structure obtained from the blast-buffer interactions for the interaction of a uniform wave an air-depleted buffer. Exact analytical expressions are obtained for the mitigation obtained in the incident wave momentum in terms of the incident shock pressure and the characteristics of the depleted buffer. The results obtained are verified through numerical simulations. It is found that the numerical results are in excellent agreement with the theory. The work presented could help in the design of effective blast protective materials and systems, for example in the construction of air-vacated sandwich panels.

Keywords: Blast Mitigation, Air-depleted Buffer, Low Pressure, Blast Waves, Sandwich Plates, Numerical Simulations

Thesis Supervisor: Raúl A. Radovitzky
Title: Associate Professor, Aeronautics and Astronautics

Acknowledgments

I would like to take this opportunity to extend my gratitude to all those people who have contributed to this work.

I would like to thank my academic and research adviser, Prof. Radovitzky for his invaluable guidance and motivation. He suggested an important concept to be explored, which forms the central subject of the work. Through his insights and discussions, he has helped me understand the practical relevance of the work undertaken. He has helped to bring a greater depth and clarity in my writing and communication skills. Right from the discussion of the conservation laws to making difficult career decisions, he has been a constant support. I thank him for believing in me and helping me ride successfully through the rugged road of research.

I would like to thank the director, Prof. Jaime Peraire and the ex-director, Prof. Robert Freund of the Computation for Design and Optimization program, who have provided me with the necessary guidance and the required resources to complete the program. I extend my gratitude to the administrative staff at MIT who have taken special efforts to ease me through the formal procedures.

I would like to thank the postdoctoral researchers in my group, Tan Bui and Antoine Jerusalem who have helped me through their directions and contributions, on working with the computational resources in the group and with whom I have had many useful discussions on the problem. I would like to thank the people in the RR Group, Prof. Ludovic Noels, Nayden Kambouchev, Michael Ronne Tupek, Andrew Seagraves, Michelle Nyein, Lei Qiao, Brandon Talamini, Li Yu, Amanda M. Jason, Piotr Fidkowski, Riley Schutt and Ganesh Gurumurthy for their interest and support on very important problems in the project. Not only did the lively discussions with the group help me learn, their friendly support has made my stay at MIT very memorable. I wish to acknowledge my friends, whose names would take many pages to fill, for providing me with their constant encouragement and support.

I wish to thank all my friends and family members at MIT and back home for extending their love and support in all my endeavors. I would like to remember my father

who had always encouraged me to dream beyond my abilities but unfortunately, did not live to see this moment.

Last, but not the least, I would like to thank the Department of Defense Multidisciplinary University Research Initiative (MURI) Program and the Institute of Soldier Nanotechnology established by the research branch of the United States Army for the financial support during the years.

Contents

List of Figures

List of Tables

Chapter 1

Introduction

Due to the acts of terrorism in recent years, there has been an enormous increase in the intensity of damage caused to structures and the number and the severity of human injuries. There were over one hundred terrorist incidents all over the world and around one thousand human casualties caused by these incidents this year alone [1]. Hence, there is a need to use effective blast mitigation methods in order to contain the damaging effects of terrorism. This makes the development of protective strategies for blast mitigation extremely significant and immediately important in today's society. Significant governmental, military and civilian resources have been directed towards the development of strategies for blast protection. There is an increased interest in research focusing on the design of civilian and military structures, vehicles and armor for personnel protection with improved blast resistance properties. In this chapter, we present some of the well-understood concepts about blast waves, the recent advances in the development of strategies for blast protection and the context of the present work in this field.

1.1 Explosions and Blast Waves

A chemical explosion involves the rapid oxidation of the fuel elements (carbon and hydrogen atoms) forming a part of the explosive compound resulting in a sudden release of energy over a very short period of time (in the order of a few microseconds).

The oxygen needed for this reaction is also contained within the compound so that air is not necessary for the reaction to occur. The rate of the reaction is much greater than the rate of the burning of a fuel in atmospheric air [5].

When the explosive materials decompose at a rate much below the sound of speed, the combustion process is known as deflagration. Deflagration is propagated by the liberated heat of the reaction and the flow direction of the reaction products is opposite to the direction of decomposition. If the decomposition rate of the explosive is greater than the speed of sound, the combustion process is known as detonation. Most explosives can be detonated if a sufficient stimulus is given. Detonation produces a high intensity shock wave with large pressure and temperature gradients at the shock wave front. The reaction is initiated instantaneously. The reaction rate, described by the detonation velocity, lies between 1500 and 9000 $\mathrm{m.s^{-1}}$ which is appreciably faster than the propagation speed in deflagration [16].

Most explosives in common use are condensed: they are either liquids or solids. In this work, we focus on explosions caused by the detonation of condensed blast explosives. It is common to use TNT as a reference explosive for measuring the blast parameters. The blast energy from explosives other than TNT equals a 'TNT conversion factor' times the mass of the explosive multiplied with the specific energy of TNT. Conversion factors for a number of explosives are given in literature [23].

1.1.1 Spherical explosions in air

The following discussion pertains to the case of explosions that are generated and propagate in free air remote from any reflecting surface. This case is easier to analyze than other type of explosions such as underwater explosions and hemispherical explosions.

When the explosive is detonated, it decomposes violently with the release of heat, sound and the production of gas. In air, the chemical explosive is converted almost instantaneously into explosive gases which are in a state of high pressure and high temperature. The gases expand violently and force the surrounding air out of the volume it occupies. A layer of compressed air or the blast wave, develops in front of

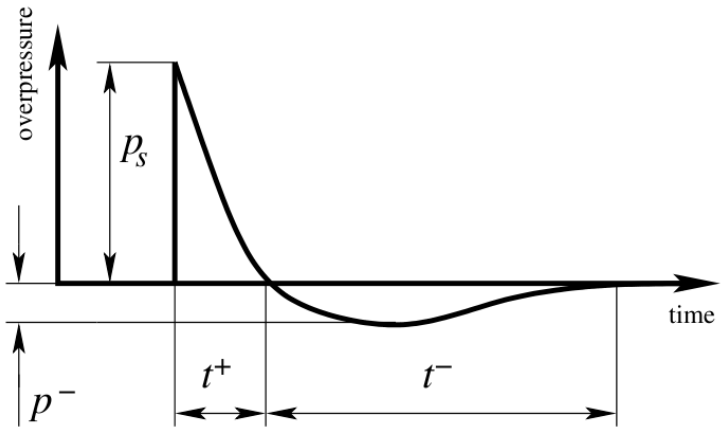

Figure 1-1: A schematic overpressure profile measured by a pressure sensor at a fixed distance from the explosion center [27].

the gases. The blast wave contains as much as 95% of the available energy. The rest of the energy is dissipated through thermal radiation and light generation [27]. For our purposes, we consider that all of the explosion energy goes into the energy of the blast wave. The fast energy release causes an instantaneous increase in the pressure and temperature of the explosive products to values that can reach 100 GPa and 3000 K respectively. The extremely high pressure within the explosion products generates a strong blast wave propagating in the surrounding medium away from the explosion center at supersonic speeds of the order of 2-3 km.s^{-1}. As the gas expands away from the source, its pressure falls to atmospheric pressure. There is a reversal of flow towards the source driven by the pressure differential between the source point and the wavefront. This induces a region of 'underpressure' in the blast wave which is seen as a 'negative phase' in the time history of the blast wave at a fixed point. Eventually the situation returns to equilibrium as the motion of the air in both directions ceases and ambient conditions are attained [12].

A typical pressure-time profile for a blast wave in free air at a fixed point in space is shown in Figure 1-1. The profile is often described by exponential functions such as the modified Friedlander equation [5].

$$p(t) = p_0 + p_s \left(1 - \frac{t}{t_+}\right) e^{-\frac{bt}{t_+}}, \tag{1.1}$$

where p_s is the peak overpressure, p_0 is the atmospheric pressure, t_+ is the decay time and b is called the waveform parameter that can be chosen to customize the pressure profile for any energy, at various distances from the source. The reference time is t_a, the time of arrival of the blast wave at the point of interest.

The specific impulse during the positive phase i_s is calculated as,

$$i_s = \text{Total impulse per unit area} = \int_0^{t^+} (p - p_0)dt. \tag{1.2}$$

The blast parameters of interest are the blast wavefront velocity, the maximum dynamic pressure, the peak static overpressure, the specific impulse of the wave and the duration of the positive phase of the wave. Of these parameters, one of the most important parameters which characterizes the blast wave is the peak static overpressure p_s.

Extensive numerical simulations have been carried out by H. L. Brode [10] to obtain empirical formulas for p_s at near and medium to far field points. The empirical formulas giving the variation of p_s with the distance from the center of spherical charge, r, measured in m, the energy released during the blast, E_i and the atmospheric pressure p_0 are given by equation 1.3.

$$\begin{aligned} p_s &= p_0 \left(\frac{C_1 E_i}{p_0 r^3} + 1 \right), && \text{if } p_s > 10p_0, \\ p_s &= p_0 \left(\frac{C_2 E_i}{p_0 r^3} + \frac{C_3 E_i^{\frac{2}{3}}}{p_0^{\frac{2}{3}} r^2} + \frac{C_4 E_i^{\frac{1}{3}}}{p_0^{\frac{1}{3}} r} - 0.019 \right), && \text{if } 0.1p_0 < p_s < 10p_0, \end{aligned} \tag{1.3}$$

with $C_1 = 0.1567$ m^3.Pa.J^{-1}, $C_2 = 0.137$ m^3.Pa.J^{-1}, $C_3 = 0.119$ m^2.Pa$^{2/3}$.J$^{-2/3}$ and $C_4 = 0.269$ m.Pa$^{1/3}$.J$^{-1/3}$.

Extensive work has been done to obtain exact expressions for the peak static overpressure in terms of the energy of the blast and the standoff distance. A scaling of the peak overpressure with the energy released during the explosion was first derived by G. I. Taylor [44], assuming that the ambient atmospheric pressure is negligable compared to the peak overpressure. Exact similarity solutions, based on Taylor's scaling were derived by John von Neumann [49] and L. I. Sedov [40]. Extensions

to these similarity solutions were derived for explosions with different initial conditions such as explosions in variable density atmosphere [41], explosions in a constant density, gamma-law atmosphere [32] and homothermic (constant temperature) flow behind the shock wave [30]. A major limitation of these similarity solutions is the assumption that the pressure of the quiescent medium is zero, which is a good approximation only for peak incident overpressures greater than 10 bar. Nonetheless, they are significant for theoretical developments. They have also formed an important basis for numerical computations of the shock flow properties which take into account the pressure of the quiescent medium [4, 39].

1.2 Blast Damage

Explosions in air create intense shock waves which reflect from the objects they intercept with reflected overpressures as high as eight times the incident overpressures, transferring huge impulses in the process and causing damage to the objects. For a structure of finite dimensions, while some part of the wave races ahead causing damage to its overpressure and impulse, the dilatational part of the wave causes suction and damage due to its underpressure. The scaling procedures and the design criteria that enable the assessment of the damage caused by blast waves to structures is given in standard references [13].

The scaling procedures and the experimental observations that enable the assessment of the intensity of the injuries and trauma that are caused to human beings by air-blast overpressures and impulses were developed in [9]. Figure 1-2 shows the survivability curves for fatality from lung damage to a human body. In the figure, m (in kg) is the weight of the man subjected to a blast wave with peak incident overpressure, p_s and specific impulse, i_s and p_0 is the atmospheric pressure. The man is assumed to be standing perpendicular to the wave in the free blast field on flat and level ground when contacted by the blast wave. This figure is a good assessment of human injury since the lungs are more susceptible to primary blast damage than any other internal organ [6]. From the figure, it is seen that the survivability of a man

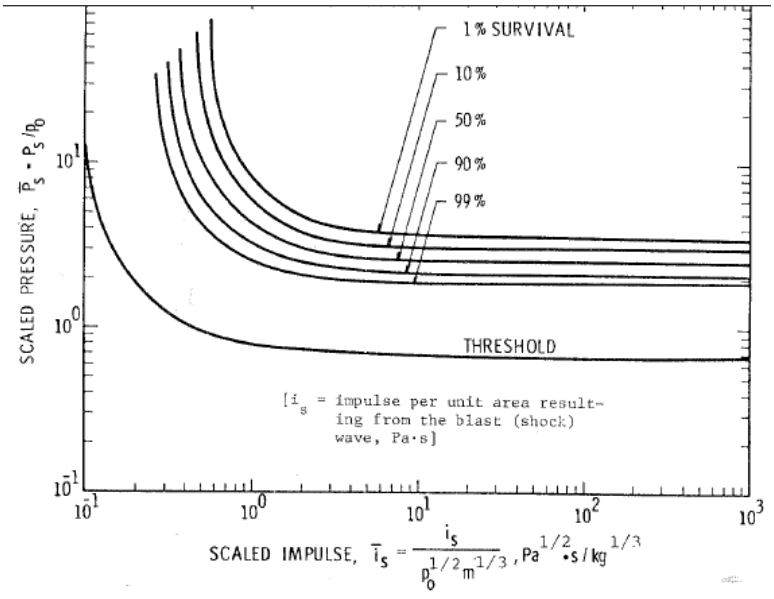

Figure 1-2: Survivability curves for lung damage to man [6].

decreases when the blast overpressure or the blast impulse increases. It is also seen that blast overpressures of the order of a few atmospheric pressures are very relevant for assessing the injuries caused to human beings.

1.3 Blast Mitigation Strategies

Numerous strategies have been investigated for mitigating the damage caused to structures due to the blast loads. A majority of the strategies are based on increasing the energy dissipation capabilities of the structure [17], increasing the mass of each individual component and using energy absorbing materials such as foam-like materials [3] and polymers [37] in the design and construction of the structures. There have also been studies based on the concept of fluid-structure interaction (FSI) for blast mitigation originating from G. I. Taylor [43]. Taylor showed that FSI can be helpful to mitigate the momentum of blast waves in the acoustic range. A main result of Taylor's studies of FSI is that light structures acquire a considerably small fraction of the free field impulse from blast waves than heavy or rigidly clamped plates. Taylor's result has been used in the design of sandwich panels with increased resistance to underwater explosions [34]. Optimized sandwich-plate designs have been predicted

to be capable of sustaining impulsive loads significantly larger than monolithic plates of equivalent weight [26]. Metallic sandwich panels with foam cores have been shown to be effective in momentum mitigation under impulsive loading for a low core to facesheet mass ratio [22]. Analytic extensions of Taylor's results in the linear acoustic limit to the non linear compressible range have recently been proposed [27, 28] which have been used to evaluate the response of metal sandwich panels to high intensity air-shocks [46]. Recently, an active deployable concept for mitigation has been shown to be beneficial for ameliorating injury to the human biological structures [51].

It is seen that a significant amount of work has been done in the design of sandwich panels utilizing the concept of fluid-structure interaction which demonstrate enhanced blast mitigation properties. A concept that has not been explored to the same level is the modification of the medium of propagation of the blast wave. The pressure of the blast waves traveling in a medium of depressed air, with pressure and density lower than ambient air, can be significantly lower than the pressure of blast waves traveling in air, depending on the depressed air pressure. The limiting case of the depressed air medium is vacuum whose pressure and density are negligable compared to air.

The mitigating effects of using vacuum as a medium of propagation have experimentally been studied in [45]. A free plate is subjected to cylindrical blasts in an air filled and evacuated spherical tank. The average deflection depth of the plate is around 9% larger in the case of air vs. vacuum, while the maximum deflection is 33% larger. The pressures experienced by the plate was higher on average for air vs. vacuum, and increased as a function of time in air due to combustion effects.

In U.S. Pat. No. 3,804,017, issued Apr. 16, 1974, D. Venable et al. [47] disclose that mitigation of the blast and shock transmission from an explosive event within a confined volume is achieved by substantially filling it with vermiculite (low density particulate energy absorbing medium) and drawing a partial vacuum into the confined volume. This invention is supported by experiments. 28 lb charges of high explosive composition were detonated in 6 ft diameter spherical confined vessels at atmospheric pressure and at a pressure of several thousand microns in a vermiculite filled vessel. The pressure rise at the wall of the vessel was less in the vermiculite filled vessel with

partial vacuum by a factor of 27 than the vessel with no filling.

Both studies are based on depleting the pressure of the medium in the entire domain from the explosive to the target. It is demonstrated that the pressure experienced by the target is lower in the case of a blast wave traveling in vacuum as compared to a blast wave traveling in air. Based on this property of an air-depleted medium, a concept is proposed that could contribute to the relief of the incident overpressure and the overpressure experienced by the target. This concept consists of incorporating an air-depleted or air-vacated buffer in the last stages of propagation of the blast wave before it interacts with the target. Interaction of the blast wave with the buffer could lead to a wave structure with lower incident pressure resulting in lower reflected overpressure and impulse on the target.

Before endeavoring to conceive ways to implement this concept, it is important to explore the concept theoretically and characterize the mitigation achieved with the depletion of the medium. In this thesis, we explore the mitigation attained through the airvacation concept of depleting the medium of propagation by reducing pressure and density of the environment next to the target. The length of the depletion is small compared to the standoff distance of the target. Numerical simulations are done to calculate the maximum pressure and the maximum impulse transferred to the target by the blast wave in air and with the depletion of the medium.

1.4 Objective

The objective of this thesis is to check the feasibility of using the concept of airvacation for the relief of blast overpressure and blast momentum in air. An understanding is sought of the influence of the blast energy and the characteristics of the air-vacated buffer on the effectiveness of the concept for mitigation. The work done could be significant in developing strategies incorporating vacated air layers for blast and injury mitigation.

Chapter 2

Numerical Studies of Airvacation Concept for Blast Mitigation

The idea of the airvacation concept is to make blast waves interact with a buffer filled with quiescent gas with pressure and density lower than ambient pressure and density, before their interaction with a target. One way to model the concept is to assume that the depressed gas is enclosed in a layer attached to the target. This layer disintegrates when the blast wave comes in contact with it allowing for the blast wave to interact with the depressed air. Numerical simulations are conducted to understand the blast-buffer interaction and study any subsequent relief of the blast impact on the target obtained by using the buffer.

The modeling approach requires an accurate representation of the flow conditions of the blast wave initialization, its propagation in air, its interaction with the air-vacated buffer and its subsequent reflection from a fixed wall. The computation is done using the computational fluid dynamics (CFD) code available as a part of the Virtual Test Facility [48]. The Virtual Test Facility (VTF) is a source code collection of compressible computational fluid dynamics and computational solid dynamics solvers. The CSD solvers provide capabilities for simulation of large plastic deformations, fracture and fragmentation in solids [19] and material response under shock wave and detonation wave loading [21]. AMROC (Adaptive Mesh Refinement in Object-oriented C++) is the fluid solver framework within the VTF software [20].

AMROC extends the capabilities of an arbitrary simple solution-routine for a conservative time-explicit finite-volume scheme formulated on a single uniform grid to a complex multi-level simulation code. The code has capabilities to simulate flows with strong shocks, fluid mixing as well as highly coupled fluid-structure interaction problems. A more detailed description of the framework and its validation with experiments for coupled blast-structure interaction problem is given in [38]. The framework supplies a generic object-oriented implementation of the special version of the blockstructured adaptive mesh refinement algorithm in [7] in C++.

2.1 Blast Initialization

During the ignition of an explosive, there is a sudden release of chemical energy from a concentrated source which leads to the formation of shock waves. The detonation process itself which leads to the formation of the blast wave is of little significance and is not modeled due to the orders of magnitude difference in the timescales of the blast wave propagation and the detonation process. This is a common modeling approach for blast waves [29, 33, 50].

In calculations leading to the blast wave initialization, there are two approaches that are commonly used. One is to assume that the shock waves resulting from the explosion form an isothermal sphere (in case of a spherical explosion) with a uniform pressure and density. The explosion energy, the initial temperature and the radius of the sphere are specified to initialize the explosion. The other is to assume that the blast waves are generated by a point source explosive. The total source energy is the only describing characteristic of the explosive. This approach is considered in our calculations.

2.1.1 Isothermal model

Brode [10] showed that it is sufficient to initialize the fluid flow variables in the volume originally occupied by the explosive as a region of uniform high temperature and pressure for an accurate representation of the initial blast wave. The expanding

gas from the sphere is assumed to have a constant specific heat γ at all stages. Given the energy released during the blast E_0, an estimated initial temperature T_i, and the initial radius of the sphere r_i, the initial pressure p_i and density ρ_i in the sphere in air are determined as per equation 2.1.

$$\begin{aligned} p_i &= \frac{3(\gamma-1)E_0}{4\pi r_i^3} + p_0, \\ \rho_i &= \frac{p_i}{RT_i}, \end{aligned} \tag{2.1}$$

where R = 287 Pa.m^3.kg^{-1}.K^{-1}, the gas constant for air and p_0 is the atmospheric pressure.

2.1.2 Point source model

In the blast wave initialization using the isothermal model described in the previous section, the blast wave shape and magnitude are assumed. A more natural description of the explosion event is based on the released explosive energy and the distance between the explosion and the target structure. The point source model is formulated around these parameters and is a more accurate way of describing the problem than the isothermal model.

This solution assumes that blast waves are produced by an ideal explosion source or by the instantaneous deposition of a fixed quantity of energy at an infinitesimal point in a uniform atmosphere. Nuclear weapons, laser sparks and condensed phase explosives can be considered as ideal explosion sources in air [5]. For an ideal explosion source it is justified to treat the central, high pressure area of the explosive as a point while modeling the initial conditions of a blast. The energy produced by ideal explosive depends only on one parameter, the total source energy E_0, irrespective of the energy density or the power source. When this finite energy is packed within a region whose volume shrinks to zero, the pressure in it theoretically rises to infinity. Under such strong shock assumptions, the initial pressure of the shock wave is pretty high and the atmospheric pressure p_0 can be neglected in comparison. This hypothesis allows the use of similarity property of the point source solution which was first

proposed by G.I. Taylor [42].The point source model presented was developed by T. Bui [11] based on the calculations presented in [39]. The solver uses a comprehensive one-dimensional finite difference scheme to solve for the flow parameters produced by spherical, cylindrical and planar blasts. The solution method is described in this section. Let s and r be Lagrangian and Eulerian coordinates of a point respectively. The equations of motion of the point in Lagrangian form are given as

$$\begin{aligned} \frac{\partial r}{\partial s} &= \frac{s^{j-1}}{r^{j-1}}\frac{\rho_0}{\rho}, \\ \frac{\partial u}{\partial t} &= -\frac{1}{\rho}\frac{\partial p}{\partial s}\frac{\partial s}{\partial r}, \\ \frac{\partial r}{\partial t} &= u, \\ \frac{\partial \cup}{\partial t} &= 0, \end{aligned} \tag{2.2}$$

where $\cup$ is some function of the entropy $\frac{p}{\rho^{\gamma}}$, j=1, 2, 3 corresponding to the planar, cylindrical and spherical symmetries. The variables s, t, p, u and r are non-dimensionalized as

$$\begin{aligned} \sigma &= \frac{s}{E^{\frac{1}{j}} p_0^{\frac{-1}{j}}};\ \ \tau = \frac{t}{E^{\frac{3}{3}}};\ \ \bar{p} = \frac{p}{p_0}, \\ \bar{\rho} &= \frac{\rho}{\rho_0};\ \ \bar{u} = \frac{u}{\sqrt{\frac{p_0}{\rho_0}}};\ \ \epsilon = \frac{r}{E^{\frac{1}{j}} p_0^{\frac{-1}{j}}}, \end{aligned} \tag{2.3}$$

where $E = E_0/\alpha_0$ where $\alpha_0 = 0.5385$, 0.9840, and 0.8510 corresponding to planar, cylindrical and spherical symmetries respectively. Introducing new variables $\tilde{p}$, θ, φ and ψ as

$$\begin{aligned} \tilde{p} &= \bar{p}^{\frac{\gamma-1}{2\gamma}};\ \ \theta = \cup^{\frac{1}{2\gamma}}, \\ \frac{2\sqrt{\gamma}}{\gamma-1}\tilde{p}\theta + u &= \theta\varphi, \\ \frac{2\sqrt{\gamma}}{\gamma-1}\tilde{p}\theta - u &= \theta\psi \end{aligned} \tag{2.4}$$

and after performing a set of operations, the equations of motion are rewritten in

terms of dependent variable φ, ψ, θ and ξ as

$$\begin{aligned}
&\frac{\partial \varphi}{\partial \tau} + \mu \frac{\partial \varphi}{\partial \sigma} + \lambda + \nu' \frac{\partial \theta}{\partial \sigma} = 0, \\
&\frac{\partial \psi}{\partial \tau} - \mu \frac{\partial \psi}{\partial \sigma} + \lambda + \nu' \frac{\partial \theta}{\partial \sigma} = 0, \\
&\frac{\partial \xi}{\partial \sigma} = \frac{\sigma^{j-1}}{\xi^{j-1}} \frac{\theta^2}{(\frac{\gamma-1}{4\sqrt{\gamma}}(\varphi+\psi))^{\frac{2}{\gamma-1}}}, \\
&\frac{\partial \theta}{\partial \tau} = 0,
\end{aligned} \tag{2.5}$$

where

$$\begin{aligned}
&\lambda = (j-1)\frac{\gamma-1}{8}\frac{\theta(\varphi^2-\psi^2)}{\xi}, \\
&\mu = \sqrt{\gamma}\left(\frac{\gamma-1}{4\sqrt{\gamma}}\right)^{\frac{\gamma+1}{\gamma-1}} \frac{(\varphi+\psi)^{\frac{\gamma+1}{\gamma-1}}\xi^{j-1}}{\theta\sigma^{j-1}}, \\
&\nu' = \frac{\varphi-\psi}{2\theta}\mu, \;\; \nu = \nu'\frac{\partial \theta}{\partial \sigma}.
\end{aligned} \tag{2.6}$$

In the first time step, when $\tau = \tau_0$, the blast is assumed to be very close to the origin and the strong shock analytical solution of Sedov [41] or Von Neumann [49] is applied in the interval [0, σ_0]. The solution is advanced in time and space by integrating the system of equations 2.5 numerically. In order to do that, the (τ, σ) plane is divided into a computational grid. The τ-axis is first divided into equal sub-intervals such that $\tau^n = \tau^{n-1} + \Delta\tau$ and then the interval [0, σ_0] is divided into k_0 sub-intervals such that $\sigma_{i+1} = \sigma_i + \Delta\sigma_{i,i+1}, i = 0, ..., k^0$. The distance the blast wave front can travel in the time Δt is given as

$$\Delta\sigma = \Delta\tau c_n, \tag{2.7}$$

where the subscript n denotes the n^{th} time step, and hence the n^{th} row in the computational grid. Therefore one computational point is added on the $(n+1)^{th}$ row so that

$$k^{n+1} = \Delta\tau k^n + 1. \tag{2.8}$$

Using the symmetry boundary conditions at the point source and the Rankine-Hugoniot conditions at the blast wave front, the non-linear PDEs from equation

2.4 are discretized and solved explicitly using the Picard iteration in each time step and advanced forward in time. At the end of each time step the flow variables can be obtained from the dependent variables as follows.

$$u_i^{n+1} = \left(\frac{\gamma - 1}{4\sqrt{\gamma}} (\varphi_i^{n+1} + \psi_i^{n+1}) \right)^{\frac{2\gamma}{\gamma - 1}}, \tag{2.9a}$$

$$p_i^{n+1} = \frac{1}{2} \theta_i^{n+1} (\varphi_i^{n+1} - \psi_i^{n+1}), \tag{2.9b}$$

$$\rho_i^{n+1} = \frac{(p_i^{n+1})^{\frac{1}{\gamma}}}{(\theta_i^{n+1})^2}. \tag{2.9c}$$

The solution can be advanced to any desired distance for planar, cylindrical and spherical blasts.

The results obtained from the point source blast model have been compared with experiments involving air blasts with spherical symmetry [8, 15]. These comparisons are shown in Figure 2-1. There is an excellent agreement between the numerical results and the experiments for important blast metrics such as the incident impulse, the reflected overpressure and the underpressure of the incident blast wave. These results show that the model accurately represents the formation and the propagation of the blast wave.

This model is a better representation of the physics of the problem than the isothermal model since the fundamental characteristics of the blast explosive are used for the initialization. The solution is initialized at the initial time step with the exact flow field as opposed to an empirical flow field in the isothermal model.

For problems involving the study of blast-target interactions, the solution for the fully formed blast wave with the blast front right next to the target can be obtained using the point source model. The solution is interpolated from the point source grid onto the computational grid of the problem of interest. Since the point source grid is one-dimensional, independent of the geometry or the dimension of the target, this model leads to huge savings in computation time and resources as compared to the isothermal model, in which the blast wave is initialized to a short distance from the center of the explosion.

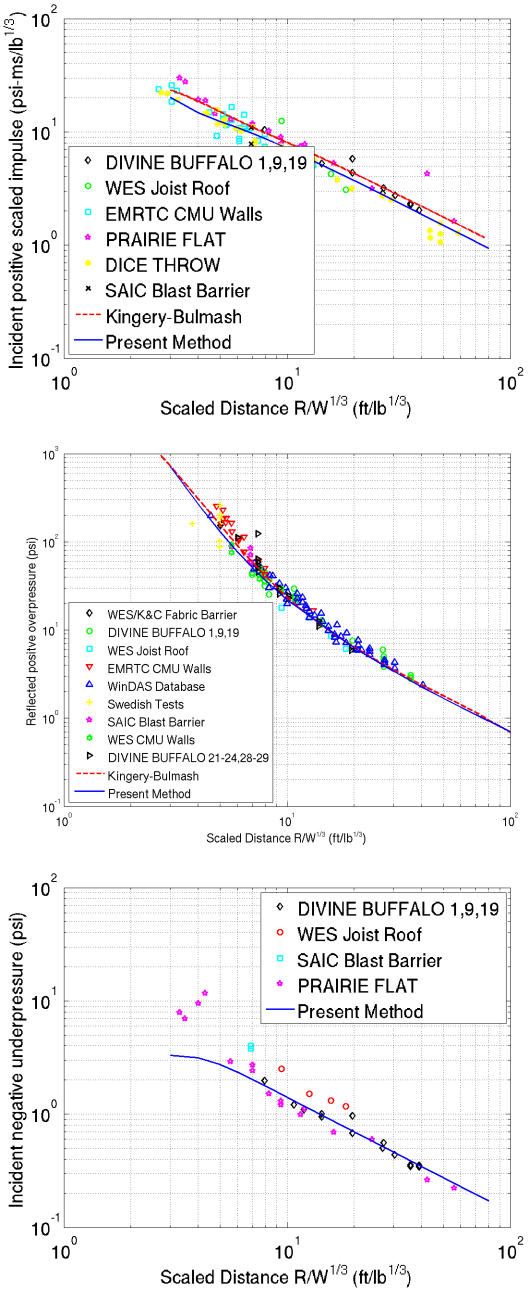

Figure 2-1: Comparison of the flow parameters obtained through the point source solution with experiments. Figures courtesy of Dr. Tan Bui.

2.2 Verification of the Code for Normal Shocks

It is important for the numerical model to be able to accurately represent the discontinuities in flow properties that arise from wave interactions in our problem. The main discontinuities in the problem arise in the form of shock waves. In this section, a verification of the capability of the code to represent shocks is done for the reflection of normal shocks from a rigid wall. A comparison is made between the reflection coefficient obtained from the code and from analytical solutions existing in the literature [2,35]. The analytical solution that is used is described in the following paragraph. Consider a shock wave reflection from a rigid boundary located at $x =$ 0m. The boundary condition is $u(x = 0, t) = 0$ m/s. An incident shock wave of pressure p_S, overpressure p_s travels in a fluid of pressure p_0 to the wall on the left, reflects from it and creates a reflected wave of pressure p_R, overpressure p_r moving to the right. It is useful to define the reflection coefficient C_R as the ratio of the reflected overpressure to the incident overpressure. Utilizing the Rankine-Hugoniot relations for a perfect gas, the reflection coefficient $C_R = p_r/p_s$ is found to be in terms of the incident shock overpressure ratio p_s/p_1 as

$$C_R = \frac{p_r}{p_s} = \frac{(3\gamma - 1)\frac{p_s}{p_0} + 4\gamma}{(\gamma - 1)\frac{p_s}{p_0} + 2\gamma}. \tag{2.10}$$

The minimum value of the reflection coefficient is 2 for $p_s/p_0 \to 0$ for all values of γ. For infinitesimal shock pressures, the fluid can be considered incompressible and the formula agrees well with acoustic linear approximation. The maximum value of the reflection coefficient is $\frac{3\gamma-1}{\gamma-1}$ for $p_s/p_0 \to \infty$ (for air with $\gamma = 1.4$, sup $C_R =$ 8). For air, the effects of compressibility become appreciable for very low incident overpressure ratios p_s/p_0 (for $p_s/p_0 = 1.0$ the reflection coefficient $C_R = p_r/p_s$ equals 2.75). Modeling shock wave propagation and reflection in air requires an elaborate numerical treatment to include effects of compressibility. The AMROC framework is used to model the normal shock wave reflection numerically. Simulations are run for incident pressure ratio p_S/p_0 ranging from 1 to a very large value of 10^4. The

shock wave has to propagate through at least one element in one time step so that no information is lost in the discretization. This condition is used to calculate the grid size.

$$\Delta x/\Delta t \leq U_s \Rightarrow (D/N)/\tau \leq U_s \Rightarrow N \geq D\tau/U_s.$$

where Δx is the grid size, Δt is the timestep, N is the total number of elements, D is the domain size, τ is the number of time steps per second and U_s is the shock speed. The values of C_R obtained from AMROC are compared with the analytical values as shown in Figure 2-2. A comparison between the analytical and numerical results for some representative values of C_R is presented in Table 2.1 ($C_R = 2$ for $p_S/p_0 = 1$ and $C_R = 7.9999$ for $p_S/p_0 = 10^5$). The comparison shows that the analytical results

Table 2.1: Reflection coefficients obtained using analytical and numerical methods.

Pressure ratio	2	5	10	20	100	10000
Numerical	2.7501	4.181849	5.376	6.384631	7.6036	7.9957
Analytical	2.7500	4.181818	5.375	6.384615	7.6037	7.9958
Relative Error %	0.0036	0.00076	0.02005	0.00025	0.0011	0.000537

match the numerical values very well. The number of significant digits considered in these calculations is 5. The L_∞ norm of the relative error percentage is 0.037. From the table, it is seen that the numerical method is highly accurate for all intensities of the incident shock waves under consideration. It is also seen that that the code is more accurate for strong shocks. The density ratio ρ_r/ρ_0 of the reflected shock wave may also be expressed as a function of the incoming overpressure ratio p_s/p_0 as

$$\frac{\rho_r}{\rho_0} = \frac{\gamma\frac{p_s}{p_0} + \gamma}{(\gamma-1)\frac{p_s}{p_0} + \gamma}\frac{(\gamma+1)\frac{p_s}{p_0} + 2\gamma}{(\gamma-1)\frac{p_s}{p_0} + 2\gamma} \tag{2.11}$$

The comparison of density ratio obtained by analytical and numerical techniques is shown in Figure 2-3 for incident pressure ratio p_R/p_0 varying from 10^0 to 10^4. There is a very good match obtained between the analytical and numerical results. The L_∞ norm of the relative error percentage is 0.3747.

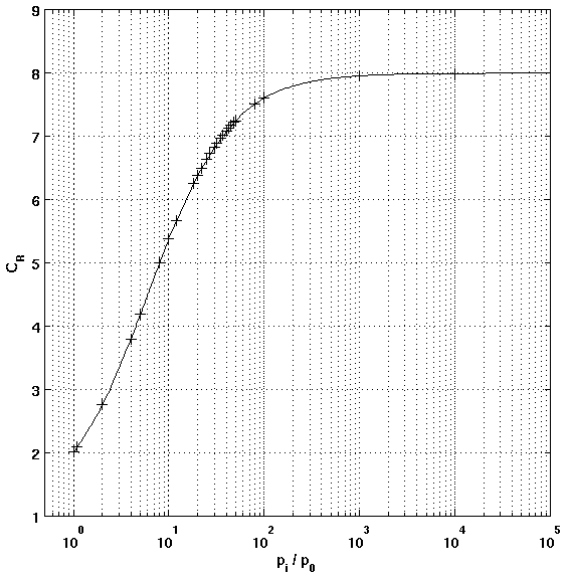

Figure 2-2: Comparison of the reflection coefficients obtained from the analytical and the numerical methods.

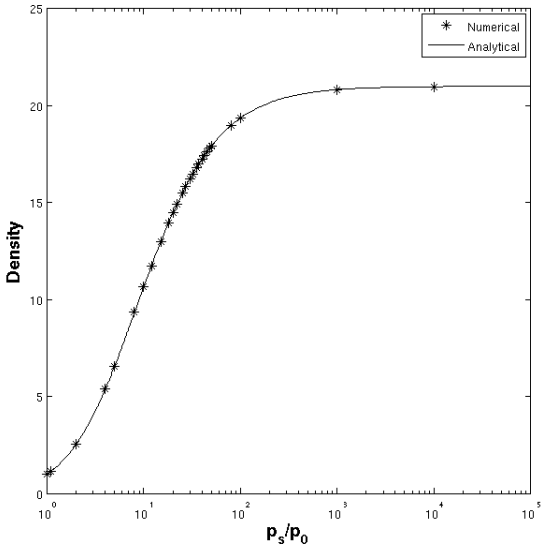

Figure 2-3: Comparison of reflection coefficients for density obtained from analytical and numerical methods.

2.3 Description of the Simulation Setup

Numerical experiments are conducted to study a possible relief obtained in the blast overpressure and the blast impulse through the interaction of a blast wave with an air-depleted buffer. The blast wave is produced by the detonation of a condensed phase explosive inside a spherical vessel. The point source model described in Section 2.1.2 is used to initialize the fully formed blast wave with the wave front right next the buffer. The flow parameters are interpolated from the point source grid to the AMROC grid using the cubic spline interpolation. The blast wave interacts directly and instantaneously with the depressed air in the buffer. As a result of the interaction of these two regions of flow, a non-trivial unsteady wave structure is expected to develop, which propagates towards the rigid wall of the vessel. It reflects from the wall with probably a much higher pressure and density. The problem has spherical symmetry, so the radial distance is the only geometric co-ordinate considered in the simulations.

The geometry of the simulation setup is illustrated in Figure 2-4. The mass of the explosive charge that generates the blast wave is M_0. The blast energy E_0, that is generated by the detonation of the charge, is calculated as described in Section 1.1. In all the calculations, the standoff distance $L = 3$m, the ambient air density $\rho_0 = 1$ kg.m^{-3}, the ambient air pressure $p_0 = 1$ atm which is approximately 10^5 Pa and the specific detonation energy of TNT = 4520 KJ.kg^{-1}. The pressure and density of the depressed air in the buffer are p_v and ρ_v respectively. The buffer length is l_v. The point source explosive and the wall are the boundary points for the simulation and symmetry boundary conditions are imposed at both the boundaries. In the computational model, the ideal gas equation of state holds for the ambient air, the buffer and the blast wave. The air and the buffer are treated as compressible fluids in which blast wave propagation is non-linear even for low shock overpressures. The entire flow is assumed to be inviscid. The values of γ in the air and the buffer are assumed to be 1.4 throughout the process, as justified by G.I. Taylor [42]. The buffer is assumed to be at the same temperature as the ambient air before the blast

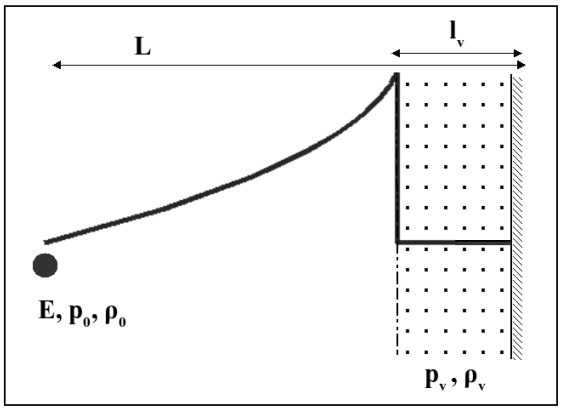

Figure 2-4: Simulation setup.

waves interacts with it. It follows that, given the buffer pressure, the buffer density can be calculated from the ideal gas equation of state, $\rho_v = \rho_0 p_v / p_0$. The buffer is initially at rest. A highly refined grid with cell size lower than 5 mm is used in all simulations. In order to capture the shock propagation with sufficient accuracy, an automatic local grid refinement comprising two levels of subdivision is applied on the grid in the cells near the shock front. A CFL number of 0.95 is used for controlling the timestep. When the CFL number increases above 1.5 during the simulations, the timestep is reduced below the initial time step of 0.2 microsec until a lower CFL number is attained. The time of interest in the simulations is the time the incident wave takes to completely reflect from the wall. It is in the order of a few milliseconds. The standoff distance is large enough to ensure no secondary reflections from the source during this time. Simulations are conducted for different blast intensities E_0, buffer lengths l_v and buffer pressures p_v. The time history of the pressure on the wall is recorded and used for further analysis. The transmitted impulse to the wall i and the transmitted specific impulse to the wall i_s are extracted from the simulations by integrating the time history of the pressure according to equation 2.12 where t_a is the time of arrival of the blast wave to the plate and t is the time of interest.

$$\begin{aligned} i_s &= \int_{t_a}^{t} p dt, \\ i &= \int_{t_a}^{t} 4\pi L^2 dt. \end{aligned} \tag{2.12}$$

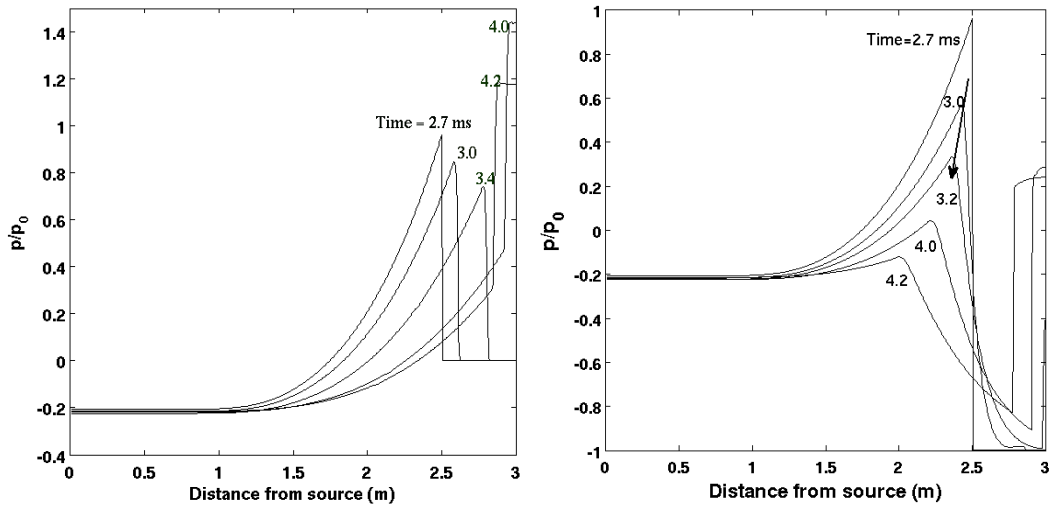

(a) Evolution of a blast wave in air

(b) Evolution of the blast wave after interacting with the buffer

Figure 2-5: Spatial distribution of the pressure of the blast wave.

The main objectives of the simulations are to investigate the nature of the wave resulting from the blast-buffer interactions, check the feasibility of using the buffer as a mitigator of blast pressure and impulse and characterize the mitigation with input parameters.

2.4 Wave Structure Obtained from the Blast-Buffer Interactions

The blast wave generated by an explosion consists of highly compressed air at the wave front traveling radially outward from the source at supersonic velocities. When the high intensity shock wave reflects from objects in its path, it reflects with a much higher pressure and transmits high impulses to the object. These pressures and impulses lead to high deformations and stresses on the object. The evolution of the blast wave in air for $E_0 = 1$kg, $L = 3$m is seen in Figure 2-5(a).

The evolution of the blast wave with time after its interaction with the buffer, for a test case with $E_0 = 1$kg, $p_v = 0.001$ atm, $l_v = 0.5$m and $L = 3$m is seen in Figure 2-5(b). When the shock wave is allowed to interact with the depleted air in the buffer,

the compressive shock wave is replaced by an expansion wave. The expansion wave travels opposite to the initial direction of propagation of the shock wave. The reflected wave overtakes the incident wave leading to a total defeat of the incident overpressure. Since, the incident overpressure is significantly low when the wave reaches the wall, it is expected that the reflected overpressure and impulse will be significantly lower compared to the reflected overpressure and impulse in air.

It is difficult to derive analytical solutions to describe the entire process exactly. If the original blast wave were uniform in magnitude, an analytical solution to describe the resulting self-similar wave structure can be obtained from the Riemann solution. This solution is described in detail in the Chapter 3. A lot of useful inferences are made by the comparison of the wave structures arising from the interactions of the constant wave and the decaying wave with the buffer.

2.5 Parametric Studies for the Blast Wave Interaction with Buffer

It was seen in the earlier section that there is a significant change in the structure of the incident blast wave after its interaction with the air-vacated buffer. To understand these interactions in a systematic manner, the parameters that influence the problem are identified and non-dimensionalized. Simulations are conducted by varying one non-dimensional group at a time.

2.5.1 Derivation of the non-dimensional groups

The important physical parameters in the problem are the energy of the explosive E_0, the standoff distance L, the ambient air pressure p_0, density ρ_0, the buffer pressure p_v and the buffer length l_v. The buffer density is given by the equation, $\rho_v = \rho_0 p_v / p_0$ and is a dependent parameter. The temperature in the air, the blast wave and the buffer is a dependent parameter and follows from the the ideal gas equation of state, $T = \frac{p}{\rho R}$. The specific heat ratio γ, is assumed to be a constant and is not included in

the non-dimensionalization. The output parameters or the metrics of the blast impact on the wall are p_{max}, the peak reflected pressure and i_{max}, the maximum impulse on the wall. The dimensions of the parameters are

$$\begin{aligned}
[E_0] &= kg.m^2.s^{-2}, \\
[L] &= m, \\
[p_0] &= kg.m^{-1}.s^{-2}, \\
[\rho_0] &= kg.m^{-3}, \\
[p_v] &= kg.m^{-1}.s^{-2}, \\
[l_v] &= m, \\
[i] &= kg.m.s^{-1}.
\end{aligned}$$

It is convenient to study the influence of the buffer pressure and the buffer length by forming one non-dimensional group containing each of them. Taking this into consideration, three sets of non-dimensional groups are formed which are shown in Table 2.2. The first set is adopted out of the three options available because it closely resembles the set of non-dimensional groups obtained for a uniform wave-buffer interaction (refer to Table 3.1 for more details). The resulting non-dimensional groups are

$$\begin{aligned}
\pi_1 &= \frac{l_v}{L}, \\
\pi_2 &= \frac{p_v}{p_0}, \\
\pi_3 &= \frac{E_0}{p_0 L^3}, \\
\pi_4 &= \frac{p_{max}}{p_0}, \\
\pi_5 &= \frac{i_{max}}{p_0^{1/2} \rho_0^{1/2} L^{3/2}}.
\end{aligned} \tag{2.13}$$

The groups which have been derived so far for the interaction of the spherical blast wave with the buffer can be extended to planar and cylindrical blast waves as well. The generalized groups are listed in equation 2.14 where k = 1, 2, 3 for planar,

Table 2.2: Non-dimensional groups for point source blast interaction with buffer.

Reference variables	Input groups	Output groups
p_0, ρ_0, L	$\frac{l_v}{L}$, $\frac{p_v}{p_0}$, $\frac{E_0}{p_0 L^3}$	$\frac{p_{max}}{p_0}$, $\frac{i_{max}}{p_0^{1/2}\rho_0^{1/2}L^3}$
ρ_0, E_0, L	$\frac{l_v}{L}$, $\frac{p_v L^3}{E_0}$, $\frac{p_0 L^3}{E_0}$	$\frac{p_{max}L^3}{E_0}$, $\frac{i_{max}}{\rho_0^{1/2}E_0^{1/2}L^{3/2}}$
p_0, ρ_0, E_0	$\frac{l_v}{E_0^{1/3}p_0^{-1/3}}$, $\frac{p_v}{p_0}$, $\frac{L}{E_0^{1/3}p_0^{-1/3}}$	$\frac{p_{max}}{p_0}$, $\frac{i_{max}}{E_0\rho_0^{1/2}p_0^{-1/2}}$

cylindrical and spherical blasts respectively.

$$\begin{aligned}
\pi_1 &= \frac{l_v}{L}, \\
\pi_2 &= \frac{p_v}{p_0}, \\
\pi_3 &= \frac{E_0}{p_0 L^k}, \\
\pi_4 &= \frac{p_{max}}{p_0}, \\
\pi_5 &= \frac{i_{max}}{p_0^{1/2}\rho_0^{1/2}L^{k-\frac{3}{2}}}.
\end{aligned} \tag{2.14}$$

E_0 and i_{max} are the blast energy and the impulse per unit area and unit length for cylindrical and planar blasts respectively. The numerical studies are divided into four different cases. The reference configuration in all the cases is the one where the blast wave propagates in air in the absence of the air-vacated buffer. In the first two cases, the blast is fixed. One buffer input is varied in each case. The pressure and the impulse histories on the wall, p_{max} and i_{max} on the wall are compared with those obtained in the reference configuration. In the third case, the buffer parameters are fixed and the blast energy is varied. The outputs of interest remain the same. One prominent observation from the studies is the existence of a threshold pressure p_{th} for each set of E_0, L and l_v. p_{max} and i_{max} remain approximately the same when the buffer pressures are lowered below p_{th}. The variation of this threshold pressure p_{th}, for different blast energies is studied in the fourth case. The different cases studied are summarized in Table 2.3.

Table 2.3: Cases studied for the parametric analysis of blast mitigation using buffer.

Fixed parameters	Outputs of interest	Varied parameters
E_0, L 1kg, 3m	p_{max} and i_{max}	p_v, l_v 0.001-1atm, 0.1, 0.5m
E_0, L, p_v 1kg, 3m, 0.001atm	p_{max} and i_{max}	l_v 0.1-0.5m
p_v, l_v, L 0.001atm, 0.1m, 3m	p_{max} and i_{max}	E_0 0.1-10kg
l_v, L 0.3m, 3m	p_{th}	E_0 0.7, 1, 3kg

2.5.2 Variation of the buffer pressure

The buffer pressure p_v is varied from 0.001 atm to 1 atm in equal steps on the logarithmic scale i.e. $p_v = 0.001$, 0.01, 0.1 and 1 atm with $M_0 = 1$kg, $L = 3$m and $l_v = 0.5$m. Simulations are run on the setup described in Section 2.3 with these parameters.

It was seen in Section 2.4 that when a blast wave interacts with the air-vacated buffer ($p_v = 0.001$atm), it decomposes into a lower intensity shock wave and a rarefaction wave. Consider an infinitesimally small control volume drawn around the shock front of the incident blast wave. In order for the conservation laws described in equations (3.22a) - (3.22c) to hold in this control volume, the strength of the shock front has to change. In other words, the buffer medium cannot sustain the propagation of the same shock wave that propagates in ambient air. This leads to the formation of a shock wave with lower pressure and density than the original wave. A rarefaction wave also starts to develop in the place of the original blast wave. This wave structure continues propagating towards the wall. The spatial distributions of the incident wave pressures just before their reflections from the wall are shown in Figure 2-6. The shock front and the rarefaction wave are connected by a contact discontinuity which is noticed in the spatial density distributions just before reflection in Figure 2-7. Across a contact discontinuity, the pressure and the velocity are

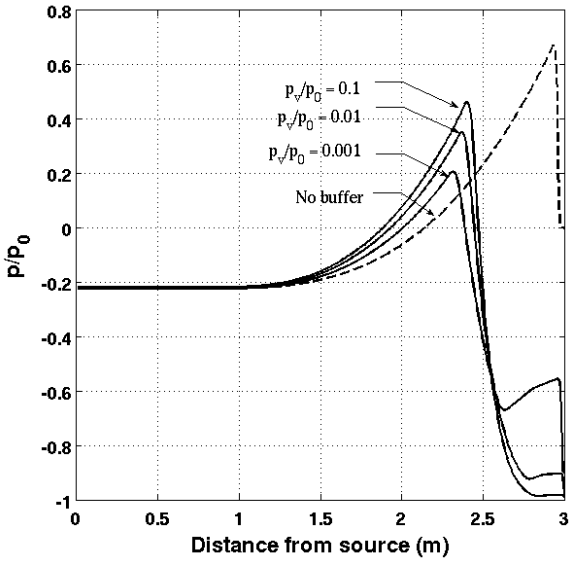

Figure 2-6: Incident overpressure profiles just before reflection, $l_v = 0.5$m.

continuous while there is a jump in the density and the speed of sound. Hence the discontinuity is not seen in the incident pressure distributions.

For p_v varying from 0.01 atm - 0.001 atm, the waves formed from the blast-buffer interactions have a similar wave structure comprising of a shock wave, a contact surface and an expansion wave. The shock wave intensity reduces as the buffer pressure reduces which leads to lower intensities and decay times of the reflected pressures. The reflected overpressure history on the wall is plotted for different buffer pressures in Figure 2-8(a). The reflected overpressure intensities experienced by the wall are of much lower magnitude in the buffer configuration as compared to the reference configuration. For a buffer pressure of 0.1 atm, two local maxima are clearly seen in the reflected pressure history. Comparison of the reflected pressure history with the incident pressure distribution shows that the first local maximum is produced by the low intensity shock wave. The rest of the reflected wave structure is produced by the complex, non-linear interactions of the reflected wave with the rest of the incident wave. Since the intensity of the incident waves are lower in the presence of the air-vacated buffer, the peak reflected overpressures on the wall are lower. For $p_v = 0.001$ atm, the strength of the incident shock wave is so low that the reflected pressure history is smooth with no significant discontinuities. The maximum reflected pressure in

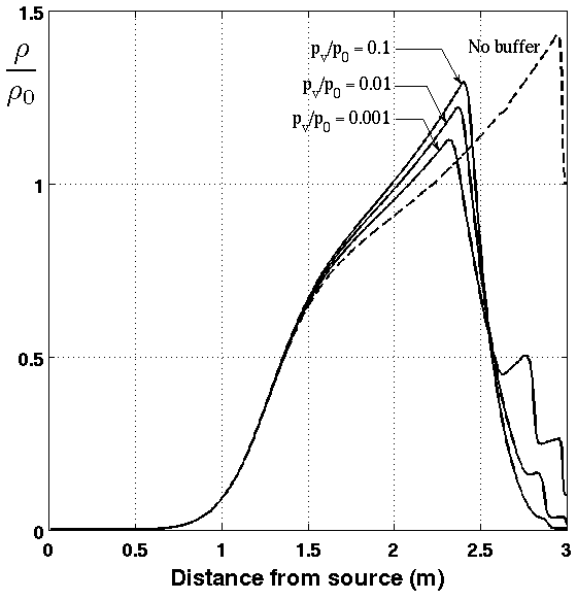

Figure 2-7: Incident density profiles just before reflection, $l_v = 0.5$m.

the reference configuration is attained the moment the incident wave starts reflecting from the wall. On the contrary, the reflected pressure in the buffer configuration increases from the low value of the buffer pressure to the peak value over a period of time. This period of time is of the order of a few milliseconds when $p_v = 0.001$atm.

The impulse experienced by the wall for different buffer pressures is compared with the reference configuration in Figure 2-8(b). In the reference configuration, the impulse increases from zero as the pressure builds up on the wall. The impulse attains its maximum value when the pressure decays back to 1 atm and the negative phase in the reflected pressure profile starts. In the free field interactions of a spherical blast wave with a target, the impulse decreases to its minimum value when the negative phase of the pressure wave is completed. In the presence of a buffer, the impulse starts to decrease below zero. This is because the reflected pressure on the wall builds from the negative values of the buffer overpressures. When the pressure reaches 1 atm, the impulse attains a local minimum. As the pressure continues to build towards its peak value, the impulse starts to increase again. When the negative phase of the reflected pressure starts, the impulse attains its local maximum and starts to decrease. The impulse in the free-field interactions of the blast wave with a target is expected to

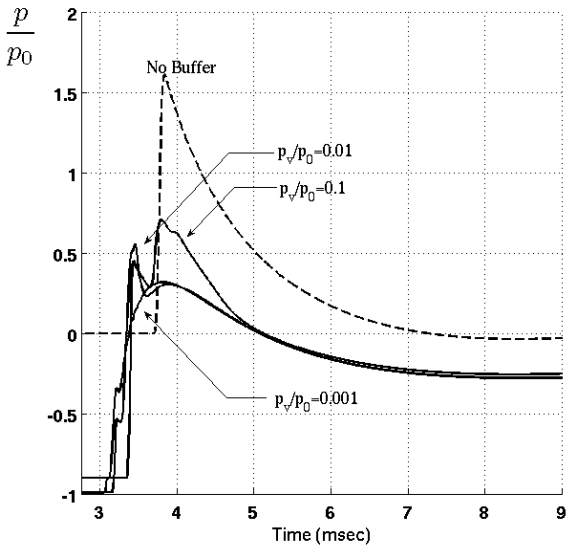

(a) Reflected Overpressure History on the Wall

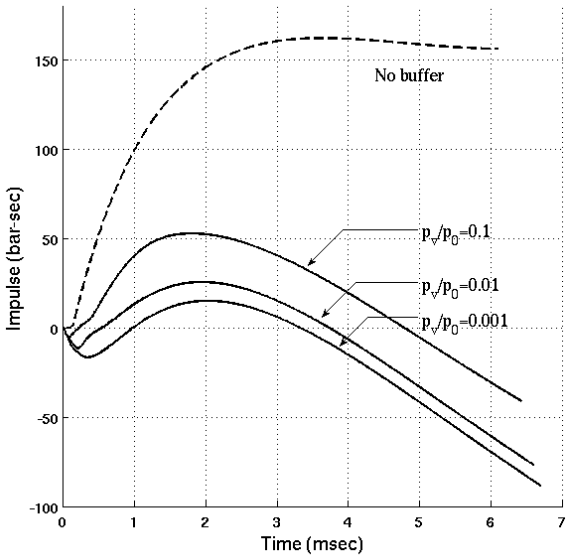

(b) Impulse Exerted on the Wall

Figure 2-8: Reflected pressure and impulse histories on the wall for different buffer pressures, $l_v = 0.5$m. the time scales in the impulse and pressure figures are different since impulse is calculated from the time the wave is reflected from the wall.

Table 2.4: Pressure and impulse relief through air-vacated buffer, E_0=4520 KJ, L = 3m, l_v = 0.5m, p_{max}, i_{max}, p_{0max} and i_{0max} are the peak reflected overpressures and impulses on the wall in the buffer and the reference configuration respectively.

Buffer pressure $\frac{p_v}{p_0}$	Reflected pressure $\frac{p_{max}}{p_0}$	Mitigation $\frac{p_{max}-p_{0max}}{p_{0max}}(\%)$	Impulse $\frac{i_{max}}{i_{0max}}$	Mitigation $\frac{i_{max}-i_{0max}}{i_{0max}}(\%)$
1e0	161338	0.0	00162.4	00.0
5e-1	135455	16.0	00107.0	34.1
1e-1	70969	56.0	00058.2	64.2
5e-2	70508	56.3	00045.8	71.8
1e-2	56029	65.3	00037.1	77.2
5e-3	34398	78.7	00034.1	79.0
1e-3	32076	80.1	00031.7	80.5

follow the decreasing trend and attain its minimum value when the negative phase of the pressure wave is completed. It is to be noted that the time scales in the impulse and the pressure plots are different since the impulse is calculated from the time the wave starts reflecting from the wall. For example, a time of 3 millisec on the impulse plot for p_v = 0.001 atm corresponds to a time of 6 millisec on the pressure plot. In general, in the presence of the depleted buffer, the intensities of the impulses acting on the wall and i_{max} are much lower in the buffer configuration as compared to the reference configuration.

The maximum reflected overpressures and the impulses for each of the buffer pressures is summarized in Table 2.4. Even for a buffer pressure as high as 0.1 atm, there is a 50% reduction in the peak reflected pressure. For a buffer pressure of 0.001 atm, there is a significantly high 80% reduction in the peak reflected pressure and the maximum impulse acting on the wall. These numbers clearly show that using an air-vacated buffer reduces the intensities of the reflected pressures and the reflected impulses. Blast damage caused to structures or part of structures is due to the pressure exerted by the blast wave or due to the impulse exerted by the blast wave or both depending on the intensity of the blast wave and the natural response time of the structure. Also, the survivability of a person from lung damage improves tremendously by reducing both the pressure and the impulse of the blast wave (refer to Section 1.2 for more details). Thus, it is expected that using the airvacation

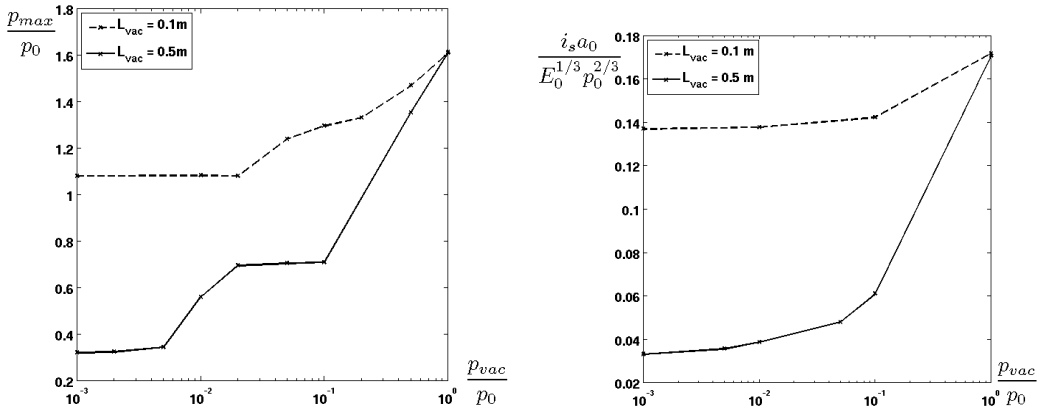

Figure 2-9: Peak reflected overpressures and maximum impulse as a function of buffer pressures.

concept in protective strategies could potentially contribute to the reduction of the blast damage caused to structures and human beings to a great extent.

The maximum reflected pressures and impulses are plotted against the buffer pressure in Figure 2-9. It is seen that there is a negligable change in p_{max} and i_{max} when the buffer pressures are reduced beyond a certain value. In other words, there is a limit to the reduction of the pressure and impulse that can be achieved for a given E_0 and l_v. We refer to the maximum buffer pressure at which this limit is achieved as the threshold buffer pressure, p_{th}. For a buffer length of 0.1m, p_{th} is around 0.01 atm. This property can be used to choose a buffer pressure with the maximum mitigation to cost ratio. For a buffer length of 0.5 m, p_{th} is around 0.001 atm. The threshold buffer pressure is observed to decrease with an increase in the buffer length. A decrease in the buffer length decreases the reduction limit that can be achieved in the overpressure and the impulse. This limit can be used to choose a buffer length to achieve the desired overpressure and impulse mitigation.

2.5.3 Variation of the buffer length

The buffer length l_v is varied from 0m to 0.5m in equal steps of 0.05m with p_v = 0.001 atm, E_0 = 1kg and L=3m. The reflected overpressure histories on the wall for different buffer lengths are shown in Figure 2-10. It is observed that the reflected

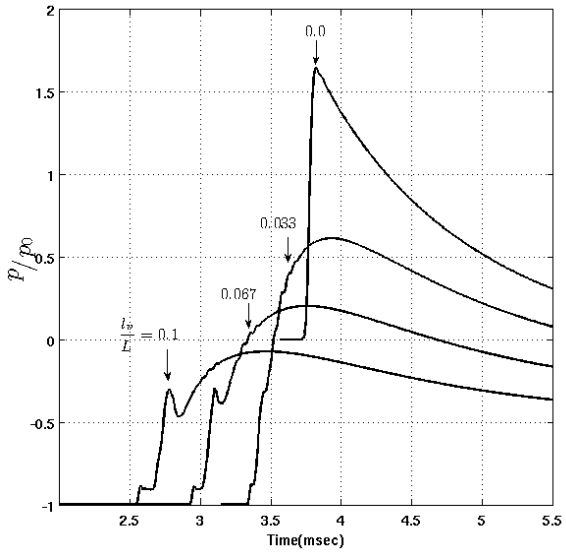

Figure 2-10: Reflected overpressure history on wall, $p_v = 0.001$ atm.

pressure waves have a similar shape for different buffer lengths. This suggests that the peak reflected overpressures might be scalable with the non-dimensional distance, l_v/L. The peak reflected pressures and impulses relative to the reference values are plotted with buffer length in Figure 2-11. It is seen that there is a huge reduction of up to 60% in p_{max} for a buffer length ratio as low as 0.16. A polynomial approximation of order two for the impulse for the data points obtained through the simulations gives a good fit as seen in Figure 2-12. Equation 2.15 gives the quadratic fit where x $= l_v/L$ and y $= i_{max}/i_{0max}$.

$$y = 9.74x^2 - 6.74x + 1. \tag{2.15}$$

2.5.4 Variation of the blast energy

The blast energy E_0 is varied from 0.5 kg to 10 kg with $L = 3$m, $p_v = 0.001$ atm and $l_v = 0.3$m. The relative peak reflected pressure versus the blast energy is plotted in Figure 2-13. One important observation is that the overpressure and impulse relief obtained by the airvacation concept is not restricted to a single energy or incident overpressure. There is a significant mitigation obtained for all the energies considered.

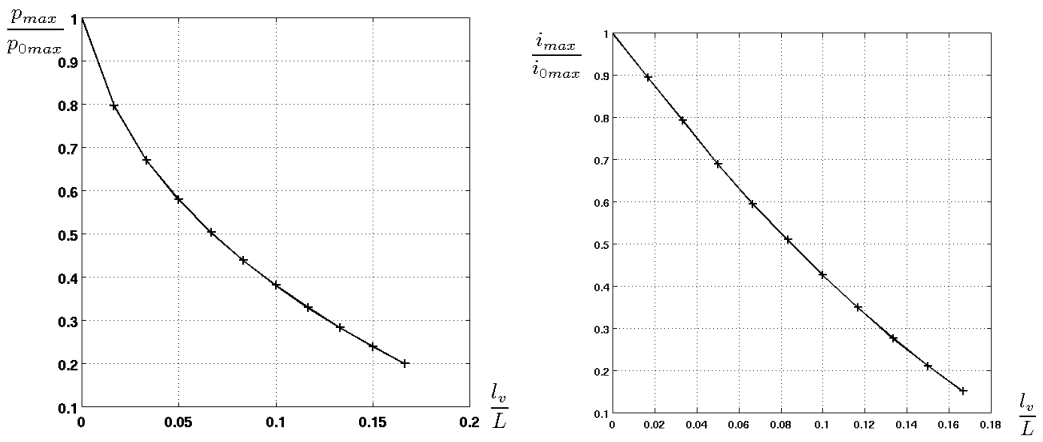

Figure 2-11: Peak reflected overpressures and maximum impulse exerted on the wall as a function of buffer length.

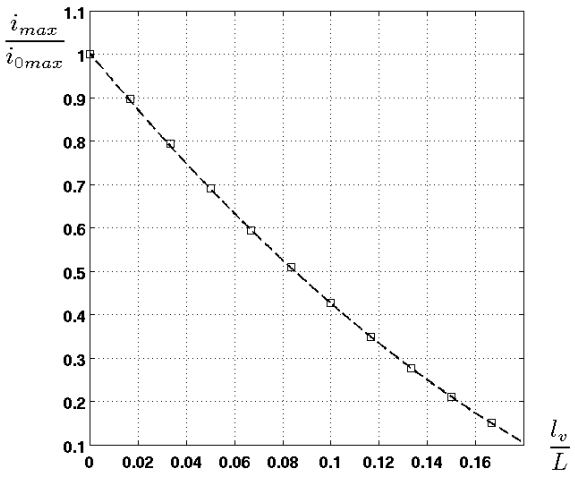

Figure 2-12: Maximum impulse exerted on the wall as a function of buffer length. The dotted line is the quadratic fit of the data points that were obtained through the simulations.

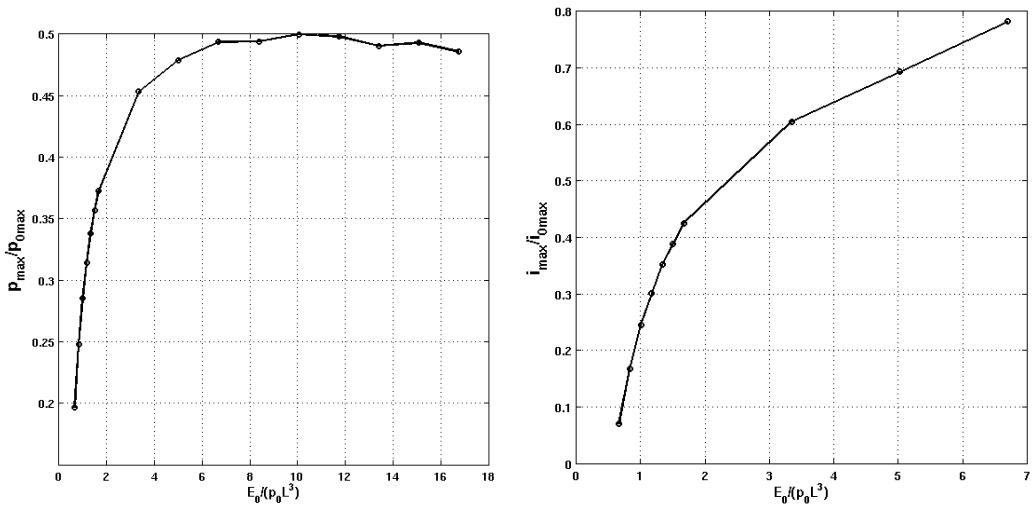

Figure 2-13: Peak reflected overpressure and maximum impulse exerted on the wall as a function of blast energy, $l_v = 0.3$ m, $p_v = 0.001$ atm.

There is a greater reduction of impulse and pressure for lower energies. For the range of energies considered, the incident overpressures p_{inc} vary from 0.3 atm to 3.4 atm. As p_{inc} increases above 3 atm, it is observed that i_{max}/i_{0max} increases to 1, which is the limit value of mitigation for a no-buffer configuration. It is also observed that p_{max}/p_{0max} attains a limit value of 0.5 and remains almost the same. The buffer layer is effective for impulse relief for incident overpressures in the order of a few atmospheres. This order of incident overpressures is relevant to human injury from lung and brain injury from the blast overpressures. Based on Figure 1-2, a free-air blast overpressure of 3.4 atm at a standoff distance of 3m corresponds to a 1% chance of fatality from lung damage for a 60 kg person. The airvacation concept may help in design of methodologies to mitigate injury to the lungs [9] and the injury caused to the brain due to blast overpressure [36]. Figure 2-14 shows the peak reflected overpressure and impulse versus the blast energy. There is a near linear relationship between the reflected pressures and the blast energy. This suggests that a natural way of non-dimensionalization for energy is p_{max}/p_0 and $i_{max}/p_0^{1/2}\rho_0^{1/2}L^{3/2}$ rather than p_{max}/p_{0max} and i_{max}/i_{0max}. The blast energy E_0 takes values of 0.7, 1 and 3kg with $L = 3$m and $l_v = 0.3$m. The buffer pressure p_v is varied from 1 atm to 10^{-5} atm. The mitigation obtained for the peak reflected overpressures and impulses on the wall are

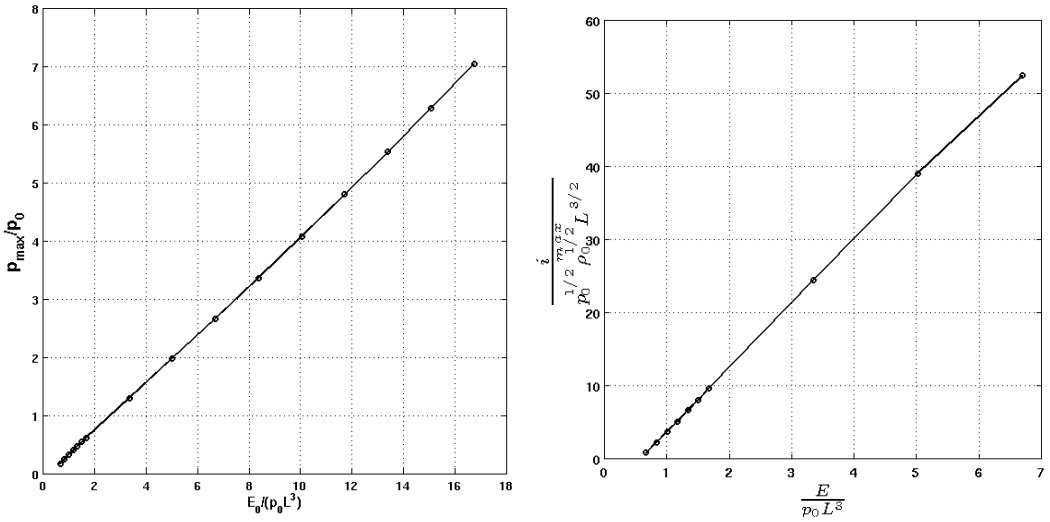

Figure 2-14: Peak reflected overpressure and maximum impulse exerted on the wall as a function of blast energy, $l_v = 0.3$ m, $p_v = 0.001$ atm.

plotted as a function of buffer pressure in Figure 2-15. A threshold buffer pressure p_{th} is seen in all the cases. The relative reflected peak pressures $p_{rmax} = p_{max}/p_{0max}$ remain almost constant for buffer pressures lower than p_{th}. When $p_v < p_{th}$, the reflected pressure histories on the wall remain almost the same leading to constancy in the relative maximum impulse $i_{rmax} = i_{max}/i_{0max}$. It is seen from the figures that p_{th} is almost the same for all the three energies ($= 10^{-3}$atm). For the cost of providing p_{th} in the air-vacated buffer, maximum relief in p_{max} and i_{max} is seen for a large range of energies, as long as the incident overpressures are of the same order.

2.6 Summary of Results

The numerical studies of the blast interaction with the air-vacated buffer firmly establishes that using an air-vacated buffer as a partial medium of propagation reduces the metrics for blast damage such as the peak reflected overpressure and the maximum impulses on the wall. The lower the buffer pressure and higher the buffer length, the better is the overpressure and impulse relief obtained. There is a threshold on the relief that is obtained by decreasing in buffer pressure for a given blast energy and buffer length. The threshold buffer pressure decreases with an increase in buffer

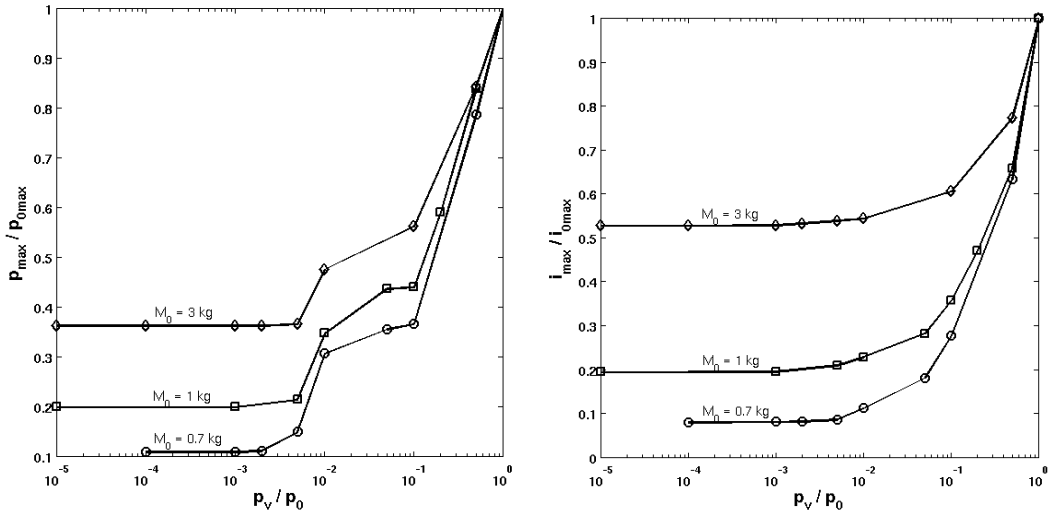

Figure 2-15: Peak reflected overpressures and maximum impulse as a function of buffer pressures for three different blast energies.

length and is invariant for the range of energies considered. There is a monotonic increase in the relief that is obtained with an increase of buffer length for a given blast energy and buffer pressure. The buffer layer is effective for impulse relief for incident overpressures in the order of a few atmospheres. This makes the concept very relevant for design of protection systems for the human body and injury mitigation. The parametric analysis that has been done in this chapter is important since the changes in the level of mitigation that can be provided with changes in the design parameters such as the buffer pressure and the buffer length have been analyzed.

Air-depleted sandwich panels

A strategy that could be suggested for blast mitigation, based on the airvacation concept is using the depressed air as a filler material in honeycomb sandwich structures used for blast protection. Air is drawn out of the cells of the sandwich structure to create a partial vacuum in the spaces between the cells. The mechanism through which the vacated cells are expected to relieve blast overpressure is illustrated in Figure 2-16. The blast wave comes in contact with the front face of the cell of a sandwich panel. The facesheet shears at the nodes of the panel or undergoes deformations depending on the intensity of the blast wave and the properties of the honeycomb structure, causing it to collapse into the cell. The depressed air in the buffer between

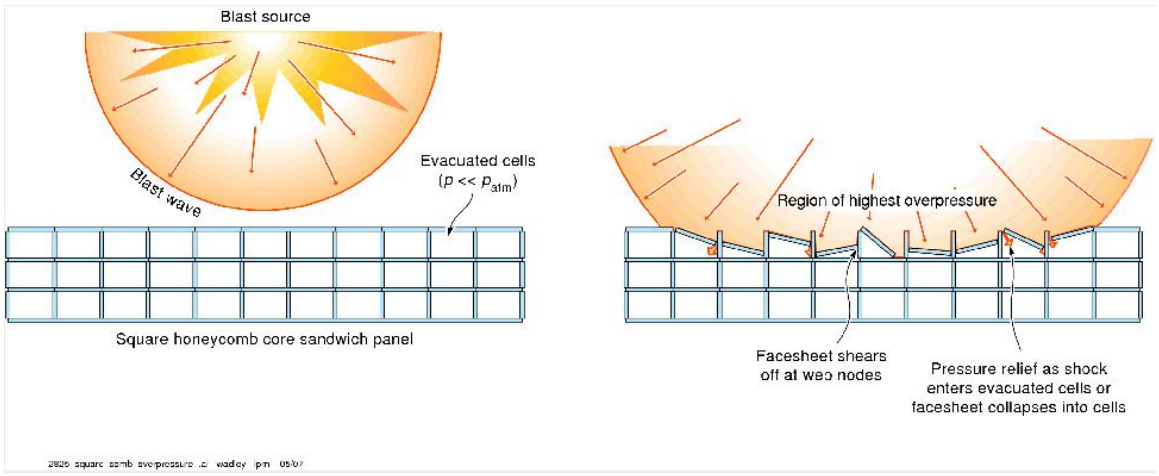

Figure 2-16: Schematic of relief mechanism in air-vacated sandwich panels. Figure courtesy of Prof. H. N. G. Wadley, University of Virginia.

the front and the back face of the cell is exposed to the blast wave. The blast wave interacts with the buffer causing a wave structure of low shock intensity to develop which relieves the incident overpressure in the blast wave. The wave structure then interacts with the back face of the cell and causes it either to shear or to deform. This pattern of interactions continues until the blast wave deforms the entire panel before interacting with the target. A large fraction of the blast energy and blast momentum is mitigated through the deformations of the cells and the buffer. The strength of the incident wave is highly reduced by the time it reaches the target. This subsequently might lead to lower reflected overpressures and transmitted impulses on the target, thus mitigating the damage caused to the target by the blast wave.

Chapter 3

Analytical Studies for Uniform Shock Interaction with the Air-Vacated Buffer

Numerical studies have shown that the interaction of the spherical blast wave, produced by a point source explosive, with an air-depleted buffer results in a significant reduction of the strength of the blast wave. As a first step in obtaining an analytical description for the blast-buffer interaction, the blast wave is approximated as a wave of uniform strength. This approximation is expected to yield meaningful results because the planar uniform wave and the spherical blast wave are both symmetric and dependent only on one geometrical coordinate, the distance from the center of the explosion.

In this chapter, a brief summary is given to the theory of wave propagation in a compressible medium. Specifically, the solutions for simple waves, shocks and contact discontinuities are presented. The wave structure resulting from the uniform wave-buffer interaction is presented based on the Riemann solution. Using the wave structure and the momentum conservation laws, expressions are derived for the momentum of the incident waves in 1D in the buffer configuration and the reference configuration with no buffer. It is expected that the when the momentum of the incident wave is reduced, the impulse exerted on a wall by the wave is also reduced.

These expressions are verified with solutions obtained from numerical methods. A thorough understanding of the effect of the buffer pressure, the buffer length and the shock strength on the incident wave momentum is obtained with the help of the expressions.

3.1 Fundamentals of Waves in a Compressible Fluid

In this section, the three types of non-linear waves that can propagate in a compressible fluid are presented. In this section, a subscript for a quantity in x and t denotes the derivative of the quantity with respect to x and t respectively.

3.1.1 Simple waves

For a continuous flow in a compressible medium, the flow can be assumed to be isentropic since there are no viscous forces. The Euler's equations for isentropic, `1D` flow are

$$\rho_t + u\rho_x + \rho u_x = 0, \tag{3.1a}$$

$$u_t + uu_x + \frac{p_x}{\rho} = 0, \tag{3.1b}$$

$$p = f(\rho), \tag{3.1c}$$

$$a^2 = f^{'}(\rho). \tag{3.1d}$$

The derivation that is presented here for the equations governing a simple wave follows along the lines of [18]. If $x(\sigma)$, $t(\sigma)$ represent a curve with $x_\sigma : t_\sigma = b : a$, then $df = af_t + bf_x$ is the derivative of f along this curve. In other words, f is a constant along $\frac{\partial x}{\partial t} = b : a$ and it is a characteristic direction. The direction was easily obtained since the equation had only one variable, f. For equations with two or more variables, the derivatives of the variables are linearly combined and the characteristic direction is obtained by imposing the condition that each of these variables combine in same direction as $\frac{\partial x}{\partial t}$. The Euler equations are expressed in terms of the variables u and ρ

by eliminating p. Let L_1 denote the equation for conservation of momentum and L_2 the equation for conservation of mass. A linear combination $L = \lambda_1 L_1 + \lambda_2 L_2$ ensures that derivatives of u and ρ combine in same direction as x and t. Such a direction depending on t, x and u, ρ is called as a characteristic.

$$L = \lambda(\rho_t + u\rho_x + \rho u_x) + u_t + uu_x + \frac{p_x}{\rho} = 0. \tag{3.2}$$

From equations (3.1c) and (3.1d),

$$p_x = f_x(\rho) = f_\rho(\rho)\rho_x = a^2\rho_x. \tag{3.3a}$$

Combining equations (3.3a) and (3.1b),

$$L = \lambda(\rho_t + u\rho_x + \rho u_x) + u_t + uu_x + \frac{a^2}{\rho}\rho_x, \tag{3.4a}$$

$$= \lambda\rho_t + (\lambda u + \frac{a^2}{\rho})\rho_x + u_t + (\lambda\rho + u)u_x = 0. \tag{3.4b}$$

Imposing the following condition to obtain the characteristics:

$$\frac{u + \lambda\rho}{1} = \frac{\lambda u + \frac{a^2}{\rho}}{\lambda} = \frac{x_\sigma}{t_\sigma}, \tag{3.5a}$$

$$(u + \lambda\rho)t_\sigma = x_\sigma, \tag{3.5b}$$

$$(\lambda u + \frac{a^2}{\rho})t_\sigma = \lambda x_\sigma, \tag{3.5c}$$

or

$$u = \frac{x_\sigma}{t_\sigma} - \lambda\rho, \tag{3.6a}$$

$$u = \frac{x_\sigma}{t_\sigma} - \frac{a^2}{\lambda\rho}, \tag{3.6b}$$

or

$$\lambda^2 = \frac{a^2}{\rho^2}, \tag{3.7}$$

$$\lambda = \pm\frac{a}{\rho}, \tag{3.8a}$$

$$u = \frac{x_\sigma}{t_\sigma} - a \text{ implies } \frac{x_\alpha}{t_\alpha} = (u + a), \tag{3.8b}$$

$$u = \frac{x_\sigma}{t_\sigma} + a \text{ implies } \frac{x_\beta}{t_\beta} = (u - a). \tag{3.8c}$$

The characteristic equations are

$$\frac{x_\alpha}{t_\alpha} = \frac{\partial x}{\partial t} = (u + a), \tag{3.9a}$$

$$\frac{x_\beta}{t_\beta} = \frac{\partial x}{\partial t} = (u - a). \tag{3.9b}$$

Equation (3.4b) can be rewritten as

$$L = \lambda(\rho_t + \frac{x_\alpha}{t_\alpha}\rho_x) + (u_t + \frac{x_\alpha}{t_\alpha}u_x), \tag{3.10a}$$

$$= \lambda\frac{\rho_\alpha}{t_\alpha} + \frac{u_\alpha}{t_\alpha} = 0. \tag{3.10b}$$

$$\frac{u_\alpha}{\rho_\alpha} = -\lambda \tag{3.10c}$$

Therefore, the equations corresponding to equations (3.9a) and (3.9b) in u-ρ plane are,

$$u_\alpha + \frac{a}{\rho}\rho_\alpha = 0, \tag{3.11a}$$

$$u_\beta - \frac{a}{\rho}\rho_\beta = 0. \tag{3.11b}$$

$$u_\alpha + \frac{a}{\rho}\rho_\alpha = 0, \tag{3.12a}$$

$$u + \int_{\rho'}^{\rho} \frac{a}{\rho} d\rho = 2s(\alpha) \tag{3.12b}$$

$$u + l(\rho) = 2s(\alpha), \tag{3.12c}$$

$$l(\rho) = \int_{\rho'}^{\rho} \frac{a}{\rho} d\rho. \tag{3.12d}$$

$$\text{Similarly, } -u + l(\rho) = 2r(\beta). \tag{3.12e}$$

Conventionally, $\rho^{'}$ is base density and $l(\rho^{'}=0)=0$ For ideal gases, the sound speed $a=\sqrt{\frac{\gamma p}{\rho}}$. Therefore $l(\rho)=\frac{2}{\gamma-1}a$.

$$r(\beta)=-\frac{u}{2}+\frac{a}{\gamma-1}, \tag{3.13a}$$

$$s(\alpha)=\frac{u}{2}+\frac{a}{\gamma-1}. \tag{3.13b}$$

r and s are the Riemann invariants. Along the characteristic described by equation (3.9a), $s(\alpha)$ is constant. If, in addition, it is assumed that $r(\beta)$ is constant in the entire domain, then u and a are unique along a characteristic. Hence, equation (3.9a) can be analytically integrated to obtain an explicit curve in x-t plane. Similarly if it is assumed for equation (3.9b), that $s(\alpha)$ is constant for the entire domain, then an explicit solution in x-t plane can be obtained. Combining equations (3.13b) and (3.9a), for a forward facing wave,

$$\frac{x}{t}=u+a=\text{constant along characteristics} \tag{3.14a}$$

$$\frac{u}{2}-\frac{a}{\gamma-1}=\text{constant across characteristics} \tag{3.14b}$$

Combining equations (3.13a) and (3.9b), for a backward facing wave,

$$\frac{x}{t}=u-a=2s=\text{constant along characteristics} \tag{3.15a}$$

$$\frac{u}{2}+\frac{a}{\gamma-1}=\text{constant across characteristics} \tag{3.15b}$$

Any region of flow governed by equations (3.14a)-(3.15b) is called a *simple wave*. The simple waves can be rarefaction waves or compression waves depending on the gradient of pressure across the wave. A simple rarefaction wave is a simple wave which decreases pressure and density across the wave. A simple compression wave is a simple wave which increases pressure and density across the wave. Mathematically,

$$u(x,t)+a(x,t)\leq u(y,t)+a(y,t),\ x\leq y, \qquad \text{for rarefaction waves,} \tag{3.16a}$$

$$u(x,t)+a(x,t)\geq u(y,t)+a(y,t),\ x\leq y, \qquad \text{for compression waves.} \tag{3.16b}$$

A centered simple wave is a wave in which all the characteristics originate from a single point in the x-t plane. For a simple centered backward facing wave, moving in air with flow parameters u_0, a_0, p_0 and ρ_0, from equation (3.15b)

$$u(x,t) + \frac{2a(x,t)}{\gamma - 1} = u_0 + \frac{2a_0}{\gamma - 1}, \tag{3.17a}$$

$$a(x,t) = a_0 - \frac{\gamma - 1}{2}(u(x,t) - u_0), \tag{3.17b}$$

and from equation (3.15a),

$$a(x,t) = u(x,t) - \frac{x}{t}. \tag{3.18}$$

For an ideal gas undergoing isentropic process,

$$\frac{p(x,t)}{p_0} = \left(\frac{\rho(x,t)}{\rho_0}\right)^{\gamma}, \tag{3.19a}$$

$$\frac{a(x,t)}{a_0} = \left(\frac{p(x,t)}{p_0}\right)^{\frac{\gamma-1}{\gamma}}. \tag{3.19b}$$

Combining equations (3.19b) and (3.17b),

$$p(x,t) = p_0 \left[1 - \frac{\gamma - 1}{2}\frac{u(x,t) - u_0}{a_0}\right]^{\frac{2\gamma}{\gamma-1}}, \tag{3.20a}$$

$$\rho(x,t) = \rho_0 \left[1 - \frac{\gamma - 1}{2}\frac{u(x,t) - u_0}{a_0}\right]^{\frac{2}{\gamma-1}}. \tag{3.20b}$$

3.1.2 Shocks

In non-linear waves, initial discontinuities can be smoothed out like in the propagation of centered rarefaction waves and other motions starting as perfectly continuous waves can lead to discontinuities like shocks. Shocks are spread over a very small region and have an infinite gradient of flow properties across them. The flow across a shock cannot be assumed to be isentropic since this assumption holds only when the gradients of flow properties are small and there are no friction forces. But the assumption holds over the rest of the domain. In addition, the three laws of conservation hold across the shock front. Application of these laws across the shock wave

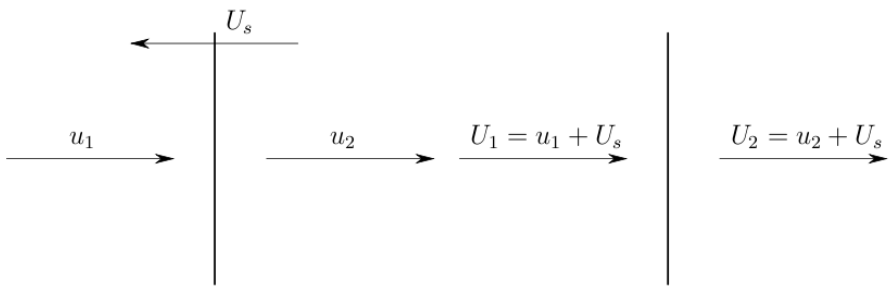

(a) Stationary reference frame

(b) Reference frame moving along with the shock front

Figure 3-1: Velocities of the shock wave and the surrounding medium in the stationary and moving reference frames.

lead to the shock jump conditions also known as *Rankine-Hugoniot* conditions. These conditions are derived along the lines of [27].

Consider a shock wave traveling with a shockfront velocity U_s as shown in Figure 3-1(a). An infinitesimally small control volume can be drawn enclosing the shock front. In a stationary reference frame, the control volume moves with the velocity U_s, which makes the analysis of the conservation laws tedious. The analysis is simplified greatly if a reference frame moving with U_s is utilized, so that the flow appears steady, as shown in Figure 3-1(b). The subscript 1 refers to the flow quantities in front of the shock and subscript 2 refers to the flow quantities behind the shock. With respect to this reference frame, the particle velocities in front of and behind the shock are

$$u_1^{'} = u_1 - U_s, \tag{3.21a}$$

$$u_2^{'} = u_2 - U_s. \tag{3.21b}$$

Application of the integral forms of the mass, momentum and energy conservation equations to a control volume which includes the shock wave gives

$$\rho_1 u_1^{'} = \rho_2 u_2^{'}, \tag{3.22a}$$

$$p_1 + \rho_1 (u_1^{'})^2 = p_2 + \rho_2 u_2^2, \tag{3.22b}$$

$$\rho_1 u_1^{'} (e_1 + \frac{p_1}{\rho_1} + \frac{(u_1^{'})^2}{2}) = \rho_2 u_2^{'} (e_2 + \frac{p_2}{\rho_2} + \frac{(u_2^{'})^2}{2}). \tag{3.22c}$$

The ideal gas equation of state applied to the regions on both sides of the shock gives

$$\begin{aligned} e_1 &= \frac{p_1}{\rho_1}\frac{1}{\gamma-1}, \\ e_2 &= \frac{p_2}{\rho_2}\frac{1}{\gamma-1}. \end{aligned} \tag{3.23}$$

Combining equations (3.23), (3.22a) and (3.22c),

$$\frac{p_1}{\rho_1}\frac{\gamma}{\gamma-1} + \frac{(u_1^{'})^2}{2} = \frac{p_2}{\rho_2}\frac{\gamma}{\gamma-1} + \frac{(u_2^{'})^2}{2}. \tag{3.24}$$

The simplest way to solve this system is to introduce the Mach number M.

$$M = \frac{u^{'}}{a}. \tag{3.25}$$

a is the speed of sound in the ideal gas given by

$$a^2 = \left(\frac{\partial p}{\partial \rho}\right)_{\text{s=constant}} = \frac{\gamma p}{\rho}. \tag{3.26}$$

Combining equations (3.25), (3.26) and (3.24),

$$a_1^2\left(1 + \frac{\gamma-1}{2}M_1^2\right) = a_2^2\left(1 + \frac{\gamma-1}{2}M_2^2\right). \tag{3.27}$$

Combining equations (3.22a) and (3.22b),

$$a_1\frac{1+\gamma M_1^2}{M_1^2} = a_2\frac{1+\gamma M_2^2}{M_2^2}. \tag{3.28}$$

Combining equations (3.27) and (3.28),

$$M_2^2 = \frac{1 + \frac{\gamma-1}{2}M_1^2}{\gamma M_1^2 - \frac{\gamma-1}{2}}. \tag{3.29}$$

From equation (3.22a),

$$\frac{\rho_2}{\rho_1} = \frac{u_1^{'}}{u_2^{'}}, \tag{3.30a}$$

$$= \frac{M_1 a_1}{M_2 a_2} \text{ (From equation (3.25))}, \tag{3.30b}$$

$$= \frac{M_1^2(1+\gamma M_2^2)}{M_2^2(1+\gamma M_1^2)} \text{ (From equation (3.28))}. \tag{3.30c}$$

Combining equations (3.30c) and (3.29),

$$\frac{\rho_2}{\rho_1} = \frac{(\gamma+1)M_1^2}{2+(\gamma-1)M_1^2}. \tag{3.31}$$

From equation (3.26),

$$\frac{p_2}{p_1} = \frac{\rho_2}{\rho_1}\frac{a_2^2}{a_1^2}. \tag{3.32}$$

Combining equations (3.32), (3.31) and (3.28),

$$\frac{p_2}{p_1} = 1 + \frac{2\gamma}{\gamma+1}(M_1^2 - 1). \tag{3.33}$$

Consider the case of shock wave traveling with speed U_s propagating in still atmosphere, $u_1 = 0\,\text{m/s}$. The shock parameters are denoted by subscript s and atmospheric parameters are denoted by subscript 0. Equation (3.31) gives

$$M_0 = \frac{-U_s}{a_0}. \tag{3.34}$$

Let $\gamma_2 = \gamma + 1$ and $\gamma_1 = \gamma - 1$. Then equation (3.31) gives

$$\frac{\rho_s}{\rho_0} = \frac{\gamma_2 M_0^2}{2+\gamma_1 M_0^2}. \tag{3.35}$$

Equation (3.33) gives

$$\frac{p_s}{p_0} = 1 + \frac{2\gamma}{\gamma_2}(M_0^2 - 1). \tag{3.36}$$

It is often useful to express the particle velocity, the shock speed and the jump conditions in terms of blast overpressure $p_s - p_0$ eliminating Mach number M_0. The

shock speed can be obtained from equation (3.21a) as

$$U_s = -a_0 M_0 = -\sqrt{\frac{p_0}{\rho_0}}\sqrt{\frac{\gamma_2}{2}\frac{p_s - p_0}{p_0} + \gamma}. \tag{3.37}$$

The particle velocity in the shock wave can be obtained from equation (3.21b) as

$$u_s = U_s + a_s M_s = -\frac{p_s - p_0}{p_0}\sqrt{\frac{p_0}{\rho_0}}\sqrt{\frac{1}{\frac{\gamma_2}{2}\frac{p_s - p_0}{p_0} + \gamma}}. \tag{3.38}$$

The jump condition for the density is obtained from equations (3.35) and (3.36).

$$\frac{\rho_s}{\rho_0} = \frac{2\gamma + (\gamma+1)\frac{p_s - p_0}{p_0}}{2\gamma + (\gamma-1)\frac{p_s - p_0}{p_0}}. \tag{3.39}$$

The jump conditions for the sound speed is obtained from equations (3.32) and (3.39).

$$\frac{a_s^2}{a_0^2} = \frac{p_s}{p_0}\frac{\frac{\gamma_2}{\gamma_1} + \frac{p_s}{p_0}}{1 + \frac{\gamma_2}{\gamma_1}\frac{p_s}{p_0}}. \tag{3.40}$$

The shock speed can be obtained in terms of the particle speed of the shock. From equation (3.21b),

$$\begin{aligned}
u_s &= U_s + a_s M_s, && \text{(3.41a)}\\
&= a_s M_s - a_0 M_0, && \text{(3.41b)}\\
&= \left(\frac{\rho_0}{\rho_s} - 1\right) a_0 M_0, && \text{(3.41c)}\\
&= a_0 M_0 \left(\frac{2 + (\gamma-1)M_0^2}{(\gamma+1)M_0^2} - 1\right), && \text{(3.41d)}\\
&= \frac{2a_0}{\gamma_2}\left(\frac{1}{M_0} - M_0\right), && \text{(3.41e)}\\
&= \frac{2a_0}{\gamma_2}\left(-\frac{a_0}{U_s} + \frac{U_s}{a_0}\right). && \text{(3.41f)}
\end{aligned}$$

Solving this quadratic equation for U_s in terms of u_s gives

$$U_s = \frac{\gamma_2 u_s}{4} + \sqrt{\frac{\gamma_2^2 u_s^2}{16} + a_0^2}. \tag{3.42}$$

3.1.3 Contact discontinuities

Contact discontinuities are surfaces separating two parts of a medium without any flow of gas through the surface. A contact surface can also be considered as a special case of a shock wave with a trivial solution $u_0 = u_1 = U$.

$$u_1 = u_2 = U \tag{3.43a}$$

$$u_1^{'} = u_1 - U = 0, \tag{3.43b}$$

$$u_2^{'} = u_2 - U = 0. \tag{3.43c}$$

From equation (3.22b), we have

$$p_1 = p_2. \tag{3.44a}$$

Equation (3.22c) is satisfied by the continuity of velocity across the contact discontinuity. Hence, it can be deduced that the density and the speed of sound on either side of the contact discontinuity need not necessarily be the same.

3.2 Analytical Solution for the Shock-Buffer Interaction

The analytical solution for the wave structure obtained from the interaction of uniform blast wave with an air-vacated buffer in 1D is described in this section. This solution is based on the solution for the Riemann problem, which is well known [31] and is widely used in numerical methods to provide superior wave capturing. The Riemann problem has uniform initial conditions on an infinite spatial domain except for a single jump discontinuity. It is one of the few exact solutions that exist for unsteady one-dimensional Euler equations, some others being the formation and decay of low intensity shock waves [14,24] and the reflection of plane waves from fixed surfaces [25].

Consider a one dimensional tube (a tube with properties constant along any cross section) containing two regions of fluid separated by a rigid diaphragm. The indepen-

dent variables are x and t. The rigid diaphragm located at $x = l_s$ separates a shock, at pressure, density and particle velocity p_s, ρ_s and u_s and the buffer, at pressure, density and particle velocity p_v, ρ_v and u_v. The atmospheric conditions p_0, ρ_0 and $u_0 = 0$ are given. The speed of sound in air $a_0^2 = \gamma p_0/\rho_0$ and the buffer $a_v^2 = \gamma p_v/\rho_v$ are assumed to be the same. This implies that $\rho_v = \rho_0 p_v/p_0$ is a dependent input variable. The buffer is initially at rest. The boundary conditions are inflow to the left and symmetry to the right.

If the diaphragm is instantaneously removed there is a pressure imbalance between the blast wave and the buffer causing a one-dimensional unsteady flow. The resulting wave structure contains

- a steadily moving shock,
- a steadily moving centered rarefaction wave (backward facing) and
- a steadily moving contact discontinuity separating the shock and the rarefaction wave.

The spatial distribution of the density of the incident wave is shown at a subsequent time in Figure 3-2. This figure clearly shows the separation of the incident wave into the different regions of flow upon interaction with the buffer. In Figure 3-3, the spatial distributions of the density in the domain are shown for the blast wave traveling in the reference configuration and the buffer configuration. The black color is the case of a shock wave traveling in air. The properties of the shock wave satisfy the Rankine-Hugoniot relations and subsequently a pure shock travels in air. The blue color is the case of a shock wave interacting with a buffer. The initial discontinuity does not satisfy the Rankine-Hugoniot conditions, hence the shock wave breaks into the structure illustrated and a shock wave of smaller magnitude propagates in the buffer. The smaller shock velocity is greater than the bigger shock velocity, so the incident wave hits the wall faster. But the head of the rarefaction wave is slower than the shock wave. If the shock wave is weak enough, the rarefaction wave propagates backwards. Let the particle velocity, u_s in the shock be given.[1] The other shock parameters can be found using the Rankine Hugoniot conditions. [see equations (3.42), (3.34), (3.35),

[1]It can also be assumed that shock overpressure is given

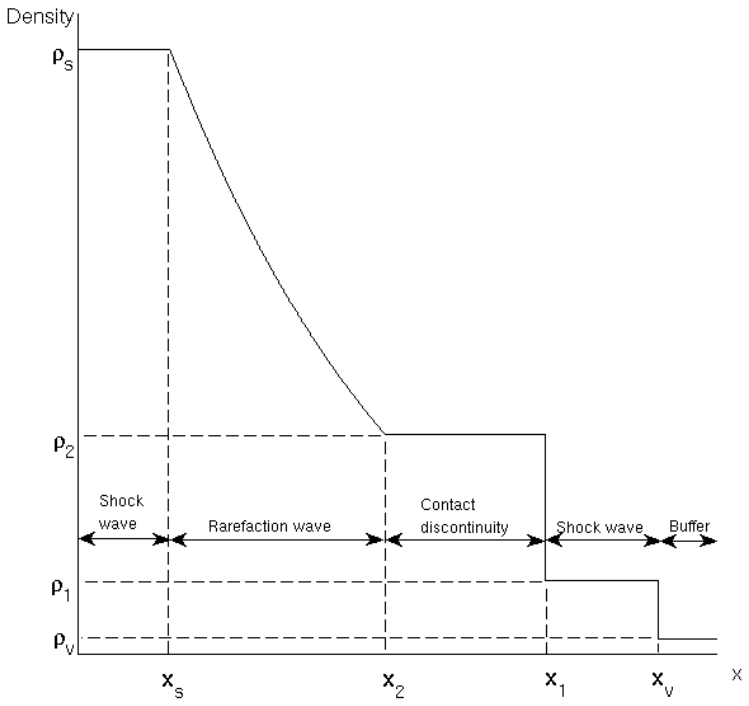

Figure 3-2: Density profile of shock wave interacting with the air-vacated buffer.

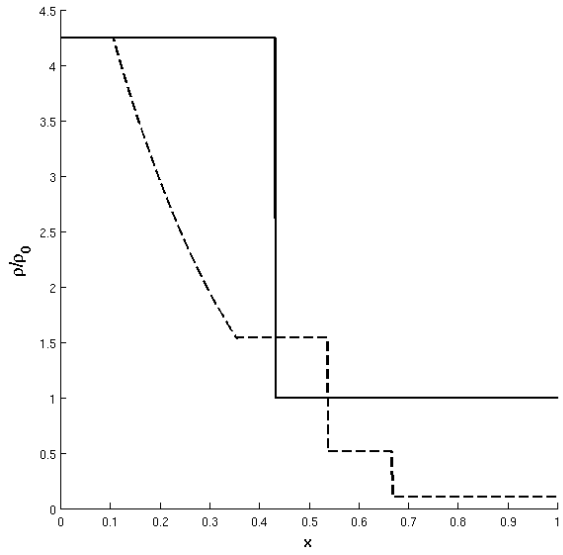

Figure 3-3: Comparison of density profiles for shock wave propagating in air and buffer. The solid line is the case of a shock wave traveling in air. The dotted line is the case of a shock wave traveling in buffer. The initial discontinuity does not satisfy the Rankine-Hugoniot conditions, hence the shock wave breaks into the structure illustrated.

(3.36)]

$$U_s = \frac{\gamma_2 u_s}{4} + \sqrt{\frac{\gamma_2^2 u_s^2}{16} + a_0^2}, \tag{3.45a}$$

$$M_0 = \frac{-U_s}{a_0}, \tag{3.45b}$$

$$\frac{\rho_s}{\rho_0} = \frac{\gamma_2 M_0^2}{2 + \gamma_1 M_0^2}, \tag{3.45c}$$

$$\frac{p_s}{p_0} = 1 + \frac{2\gamma}{\gamma_2}(M_0^2 - 1). \tag{3.45d}$$

The position of the shock front at a later time t is given by

$$x_s = l_s + (u_s - a_s)t. \tag{3.46}$$

Consider the simple centered backward facing rarefaction wave. Let the state to the right of the rarefaction wave be denoted by subscript 2 and the state of the flow along the rarefaction wave be denoted by subscript 3.

Across the characteristics of the backward facing rarefaction wave, [see equation (3.15b)]

$$u_s + \frac{2a_s}{\gamma - 1} = u_3(x,t) + \frac{2a_3(x,t)}{\gamma - 1} = u_2 + \frac{2a_2}{\gamma - 1}. \tag{3.47}$$

Combining equations (3.47) and (3.18)

$$u_3(x,t) = \frac{2}{\gamma_2}\left(\frac{x - l_s}{t} + \frac{\gamma_1}{2}u_s + a_s\right), \tag{3.48a}$$

$$a_3(x,t) = u_3(x,t) - \frac{x - l_s}{t}. \tag{3.48b}$$

Also from equations (3.19a) and (3.19b)

$$p_3 = p_s\left(\frac{a_3}{a_s}\right)^{\frac{2\gamma}{\gamma_1}}, \tag{3.49a}$$

$$\rho_3 = \frac{\gamma p_3}{a_3^2}, \tag{3.49b}$$

$$\rho_2 = \frac{\gamma p_2}{a_2^2}. \tag{3.49c}$$

The position of the head of the rarefaction wave at a later time t is given by

$$x_2 = l_s + (u_2 - a_2)t. \tag{3.50}$$

Let the state to the right of the contact discontinuity be denoted by subscript 1. [see equations (3.43a) and (3.44a)]

$$u_1 = u_2, \tag{3.51a}$$

$$p_1 = p_2. \tag{3.51b}$$

The position of the front of the contact surface at a later time t is given by

$$x_1 = l_s + u_2 t. \tag{3.52}$$

Let the state to the right of the smaller shock be denoted by subscript v and the smaller shockfront velocity be denoted by S_1. The shock density, velocity and sound speed of the shock can be expressed in terms of the shock pressure ratio ($R = \frac{p_1}{p_v}$), [see equations (3.40), (3.38), (3.39) and (3.37)]

$$\frac{a_1^2}{a_v^2} = R\frac{\frac{\gamma_2}{\gamma_1} + R}{1 + \frac{\gamma_2}{\gamma_1}R}, \tag{3.53a}$$

$$u_1 = \frac{a_v}{\gamma}\frac{R-1}{1 + \sqrt{\frac{\gamma_2}{2\gamma}(R-1)}}, \tag{3.53b}$$

$$\rho_1 = \rho_v \frac{\gamma_2 R + \gamma_1}{\gamma_1 R + \gamma}, \tag{3.53c}$$

$$S_1 = a_v\sqrt{1 + \frac{\gamma_2}{2\gamma}(R-1)}. \tag{3.53d}$$

The position of the shock front at a later time t is given by

$$x_v = l_s + S_1 t. \tag{3.54}$$

The unknown shock pressure ratio $\frac{p_1}{p_v}$ needs to be obtained in terms of known shock

pressure ratio $\frac{p_s}{p_v}$. From equation (3.49a), we have

$$a_2 = a_s \left(\frac{p_2}{p_s}\right)^{\frac{\gamma-1}{2\gamma}}. \tag{3.55}$$

Combining equations (3.55) and (3.47)

$$u_2 = u_s + \frac{2a_s}{\gamma-1}\left(1 - \left(\frac{p_2}{p_s}\right)^{\frac{\gamma-1}{2\gamma}}\right). \tag{3.56}$$

Combining equations (3.56), (3.51a) and (3.51b),

$$u_1 = u_s + \frac{2a_s}{\gamma-1}\left(1 - \left(\frac{p_1}{p_s}\right)^{\frac{\gamma-1}{2\gamma}}\right), \tag{3.57}$$

or

$$u_1 = u_s + \frac{2a_s}{\gamma-1}\left(1 - \left(\frac{p_1}{p_v}\frac{p_v}{p_s}\right)^{\frac{\gamma-1}{2\gamma}}\right), \tag{3.58}$$

or

$$\frac{p_v}{p_1} = \frac{p_v}{p_s}\left(1 + \frac{\gamma-1}{2a_s}(u_s - u_1)\right)^{\frac{2\gamma}{1-\gamma}}. \tag{3.59}$$

Finally combining equations (3.59) and (3.53b) gives,

$$\frac{p_s}{p_v} = \frac{p_1}{p_v}\left[1 + \frac{\gamma-1}{2a_s}\left(u_s - \frac{a_v}{\gamma}\frac{\frac{p_1}{p_v}-1}{\sqrt{\frac{\gamma+1}{2\gamma}\left(\frac{p_1}{p_v}-1\right)+1}}\right)\right]^{\frac{2\gamma}{1-\gamma}}. \tag{3.60}$$

Equation (3.60) gives $R = p_1/p_v$ in terms of the known shock pressure ratio p_s/p_v. The equation can be solved using iterative techniques such as the bisection method and the Newton's method. If the initial guesses are $p_1/p_v = 0.05p_s/p_v$ and $p_1/p_v = 0.5p_s/p_v$, the Newton's method converges quite rapidly. If the expression in the square brackets is negative and $\gamma > 1$, then the Newton's method fails. This difficulty is overcome by using the bisection method for solving the equation. Once R is solved, the flow parameters for the entire domain follow from equations (3.53a) – (3.49a). In some cases, the Riemann problem may yield only one or two waves or very weak

shock waves. To a large extent, the above solution procedure handles such cases automatically. It should be noted that the rarefaction wave has to remain in the domain of the stationary control volume at all times during the analysis. For very weak shocks, the rarefaction wave might propagate backwards and outside the control volume when $l_v/l_s > S_1/(u_s - a_s)$. These cases have not been considered in the analysis. The smaller shock velocity is S_1 and the length of the buffer is l_v. Hence, the time the incident wave takes to travel through the buffer and reach the wall is,

$$t_v = \frac{l_v}{S_1}. \tag{3.61}$$

The time taken by the incident wave to reach the wall when it is propagating in air is,

$$t_0 = \frac{l_v}{U_s}. \tag{3.62}$$

3.3 Control Volume Analysis for the Incident Wave Momentum

When a uniform shock wave reflects from a wall, the impulse exerted on the wall by the shock wave decreases with the incident momentum of the wave. The metric used for estimating the effectiveness of the air-vacated buffer for impulse mitigation is the ratio of the momentum of the incident blast waves in the buffer and the reference configurations.

The momentum can be obtained directly from the solution for the wave structure that is described in Section 3.2. This might not yield a closed form expression since the wave parameters are implicitly dependent on each other. A procedure utilizing the conservation of momentum in the integral form is used to derive a simple equation for the momentum contained inside the wave. The integral form of the conservation laws can be used in problems where the wave properties at the edges of the domain are of interest and the integrals of the wave properties such as the density, the pressure and the velocity are important.

Consider a control volume enveloping the entire wave in the domain. The Euler's equation for the conservation of the momentum in Cartesian coordinates in the integral form is [2]

$$\frac{\partial}{\partial t}\int\int\int_V \rho\bar{u}dV + \int\int_S (\rho\bar{u}.dS)\bar{u} = -\int\int_S pdS + \int\int\int_V \rho f dV, \tag{3.63}$$

where ρ, $\bar{u}$ and p are density, velocity and pressure, V and S denote the control volume and the control surface and f is the body force per unit mass. For one-dimensional motion with no body forces,

$$\frac{\partial}{\partial t}\int_X \rho u dX + \int_S \rho u(u.\bar{n}) = -\int_S p\bar{n}dS. \tag{3.64}$$

S denotes the left and right ends of the domain and $\bar{n}$ is the normal vector at these ends. If $\mathbf{P}(t) = \int_X \rho u dX$ denotes the total momentum in the domain at time t,

$$\frac{\partial \mathbf{P}}{\partial t} + \int_S \rho u(u.\bar{n}) = -\int_S p\bar{n}dS. \tag{3.65}$$

A control volume may be drawn enclosing the entire region from the beginning of the domain to the wall. For this control volume,

$$\frac{\partial \mathbf{P}}{\partial t} - \rho_s u_s^2 + \rho_v u_v^2 = p_s - p_v. \tag{3.66}$$

Integrating with time from initial conditions to the time the incident wave just hits the wall,

$$P_v - P_i = (p_s + \rho_s u_s^2 - p_v)t. \tag{3.67}$$

where $P_v = \mathbf{P}(\mathbf{t_v})$ is the momentum of the incident wave in the buffer configuration and $P_i = \mathbf{P}(\mathbf{0})$ is the initial momentum of the wave before it starts interacting with the buffer.

Re-arranging the equation,

$$\frac{P_v - P_i}{(p_s + \rho_s u_s^2)t_v} = 1 - \frac{p_v}{p_s + \rho_s u_s^2}, \tag{3.68a}$$

$$= 1 - \frac{p_v/p_0}{p_s/p_0 + (\gamma\rho_s/\rho_0)\left(u_s/a_0\right)^2}, \tag{3.68b}$$

$$= 1 - \frac{p_v/p_0}{\mathcal{F}(u_s/a_0)}, \text{ (From equations (3.45a) to (3.45d))} \tag{3.68c}$$

$$= 1 - \frac{\bar{p_v}}{\mathcal{F}(u_s/a_0)}, \bar{p_v} = \frac{p_v}{p_0}, \tag{3.68d}$$

$$= 1 - \frac{\bar{p_v}}{\mathcal{F}(\bar{u_s})}, \tag{3.68e}$$

where $p_s/p_0 + (\gamma\rho_s/\rho_0)(u_s/a_0)^2$ can be expressed as a function of a single non-dimensional parameter, u_s/a_0, in the function $\mathcal{F}(u_s/a_0)$ by combining equations (3.45a) to (3.45d). A similar analysis for a shock wave traveling in air yields,

$$\frac{P_0 - P_i}{(p_s + \rho_s u_s^2)t_0} = 1 - \frac{p_0}{p_s + \rho_s u_s^2}, \tag{3.69a}$$

$$= 1 - \frac{1}{\mathcal{F}(\bar{u_s})}. \tag{3.69b}$$

where $P_0 = \mathbf{P}(\mathbf{t_0})$ is the momentum of the incident wave in the reference configuration. Dividing equation (3.68a) by equation (3.69a),

$$\frac{P_v - P_i}{P_0 - P_i} = f(\bar{p_v}, \bar{u_s})\frac{t_v}{t_0}, \tag{3.70a}$$

$$f(\bar{p_v}, \bar{u_s}) = \left(1 - \frac{\bar{p_v}}{\mathcal{F}(\bar{u_s})}\right) / \left(1 - \frac{1}{\mathcal{F}(\bar{u_s})}\right). \tag{3.70b}$$

Combining equations (3.61), (3.62) and (3.70a),

$$\frac{P_v - P_i}{P_0 - P_i} = f(\bar{p_v}, \bar{u_s})\frac{U_s}{S_1}. \tag{3.71}$$

Combining equations (3.53d), (3.45a) and (3.71),

$$\frac{P_v - P_i}{P_0 - P_i} = f(\bar{p_v}, \bar{u_s}) \frac{\gamma_2 \bar{u}_s + \sqrt{2\gamma_2^2 \bar{u}_s^2 + 32}}{4\sqrt{\frac{\gamma_2}{2\gamma}(R-1)+1}}, \tag{3.72a}$$

$$\bar{u_s} = \frac{u_s}{a_0}, \tag{3.72b}$$

$$R = \frac{p_1}{p_v} = \mathcal{G}\left(\frac{p_s}{p_v}, \frac{u_s}{a_0}\right), \text{ (From equation (3.60))} \tag{3.72c}$$

$$= \mathcal{G}\left(\frac{p_s/p_0}{p_v/p_0}, \frac{u_s}{a_0}\right), \tag{3.72d}$$

$$= \mathcal{H}\left(\bar{u_s}, \bar{p_v}\right). \tag{3.72e}$$

where $R = p_1/p_v$ and $1/(4\sqrt{(\gamma_2/2\gamma)(R-1)+1})$ can be expressed as functions of the non-dimensional parameters, u_s/a_0 and p_v/p_0, in the functions $\mathcal{H}(u_s/a_0, p_v/p_0)$ and $h(u_s/a_0, p_v/p_0)$ respectively, from equation (3.60).

$$\frac{\frac{P_v}{P_0} - \frac{P_i}{P_0}}{1 - \frac{P_i}{P_0}} = f(\bar{p_v}, \bar{u_s}) g(\bar{u_s}) h(\bar{p_v}, \bar{u_s}), \tag{3.73a}$$

$$\frac{P_v}{P_0} = \frac{P_i}{P_0} + \left(1 - \frac{P_i}{P_0}\right) f(\bar{p_v}, \bar{u_s}) g(\bar{u_s}) h(\bar{p_v}, \bar{u_s}). \tag{3.73b}$$

By definition,

$$P_i = \rho_s u_s (L - l_v), \tag{3.74a}$$

$$P_0 = \rho_s u_s L. \tag{3.74b}$$

Combining equations (3.74a),(3.74b) and (3.53b)

$$\frac{P_v}{P_0} = f(\bar{p_v}, \bar{u_s}) g(\bar{u_s}) h(\bar{p_v}, \bar{u_s}) \frac{l_v}{L} + \left(1 - \frac{l_v}{L}\right), \tag{3.75a}$$

$$\frac{P_v}{P_0} = f(\bar{p_v}, \bar{u_s}) g(\bar{u_s}) h(\bar{p_v}, \bar{u_s}) k(\bar{l_v}) + (1 - k(\bar{l_v})), \tag{3.75b}$$

$$k(\bar{l_v}) = \bar{l_v} = \frac{l_v}{L}. \tag{3.75c}$$

Equation (3.75b) gives an equation for the relative momentum reduction, $P_{rv} =$

Table 3.1: Non-dimensional groups for uniform wave and point source.

Non-dimensionless Parameter	Constant Wave	Point Source Blast Wave
Length	l_v/L	l_v/L
Pressure	p_v/p_0	p_v/p_0
Energy	u_s/a_0	$E_0/(p_0L^3)$

P_v/P_0, which is the momentum of the incident wave in the buffer configuration as compared to the reference configuration. This parameter is expressed in terms of the non-dimensional buffer pressure, $\bar{p_v}$, the non-dimensional buffer length, $\bar{l_v}$ and the non-dimensional shock speed, $\bar{u_s}$. A comparison between the non-dimensional input parameters for the uniform wave and the blast wave produced by the point source explosion is made in Table 3.1. The dependence of the momentum reduction on the input parameters is studied by varying one input parameter at a time and fixing the others.

3.4 Variation of the Buffer Length

The relative momentum, P_{rv} is plotted as a function of the buffer length, l_v in Figure 3-4, for $L = 1$m, $p_s = 8.7$ atm and $p_v = 0.001$ atm. P_{rv} decreases linearly with an increase in the buffer length. If p_s and p_v are chosen in such a way that the slope of the line is high, then a small increase in the length of buffer produces a large reduction in P_{rv}. $P_{rv} = 1$ in the graph for the reference configuration (l_v =0) as expected. The value of $l_v/L = 1$ corresponds to the maximum reduction of the incident momentum that can be obtained by varying the length of the buffer for a given shock strength and a given buffer pressure.

3.5 Variation of the Buffer Pressure

The relative momentum, P_{rv}, is plotted as function of the the buffer pressure, $\bar{p_v}$ in Figure 3-5 for $p_s = 8.7$ atm, $L = 1$m and $l_v = L$. P_{rv} decreases with a decrease in the buffer pressure. $P_{rv} = 1$ in the graph for the reference configuration ($p_v = p_0$) as

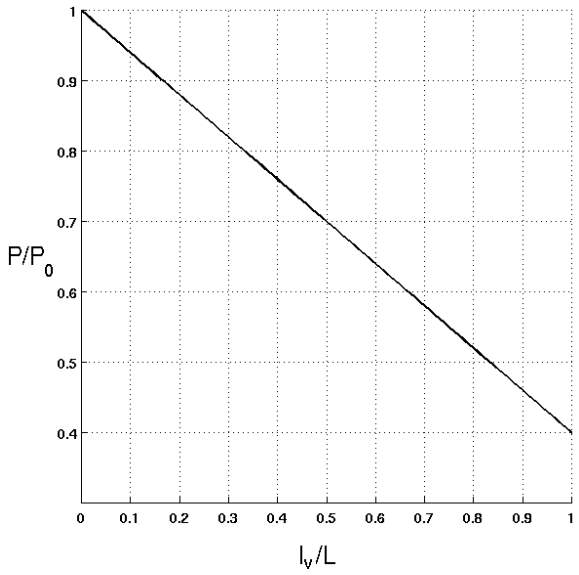

Figure 3-4: Momentum of the incident blast wave as a function of the buffer length, $p_v = 0.001$ atm, $p_s = 8.7$ atm, $L = 1$m.

expected. It is interesting to observe that P_{rv} reduces to a constant limit as p_v tends to 0. This limit value can be derived analytically. From equation (3.60),

$$\frac{p_s}{p_v} = \frac{p_1}{p_v}\left(1 + \frac{\gamma-1}{2a_s}\left(u_s - \frac{a_v}{\gamma}\frac{\frac{p_1}{p_v}-1}{\sqrt{\frac{\gamma+1}{2\gamma}\left(\frac{p_1}{p_v}-1\right)+1}}\right)\right)^{\frac{2\gamma}{1-\gamma}}, \tag{3.76a}$$

$$\left(\frac{p_v}{p_s}\right)^{\frac{1}{7}} = \left(\frac{p_v}{p_1}\right)^{\frac{1}{7}}\left(1 + \frac{\gamma-1}{2a_s}\left(u_s - \frac{a_v}{\gamma}\frac{\frac{p_1}{p_v}-1}{\sqrt{\frac{\gamma+1}{2\gamma}\left(\frac{p_1}{p_v}-1\right)+1}}\right)\right), \tag{3.76b}$$

$$\left(\frac{p_v}{p_s}\right)^{\frac{1}{7}} = \left(\frac{1}{R}\right)^{\frac{1}{7}}\left(1 + k_1\left(k_2 - k_3\frac{R-1}{\sqrt{k_4\left(R-1\right)+1}}\right)\right), \tag{3.76c}$$

$$k_1 = \frac{\gamma_1}{2a_s}, k_2 = u_s, k_3 = \frac{a_v}{\gamma}, k_4 = \frac{\gamma_2}{2\gamma}, \gamma_2 = \gamma+1, \gamma_1 = \gamma-1. \tag{3.76d}$$

$$\left(\frac{Rp_v}{p_s}\right)^{\frac{1}{7}} = 1 + k_1k_2 - k_1k_3\frac{R-1}{\sqrt{k_4(R-1)+1}}. \tag{3.76e}$$

When $p_v \to 0$, $(Rp_v)/p_s = p_1/p_s \to 0$. This is seen in Figure 3-6 where $\frac{Rp_v}{p_s}$ is plotted as a function of p_v for strong and weak shocks. This implies that the strength of the shock wave propagating in the buffer is very low when the buffer has near zero

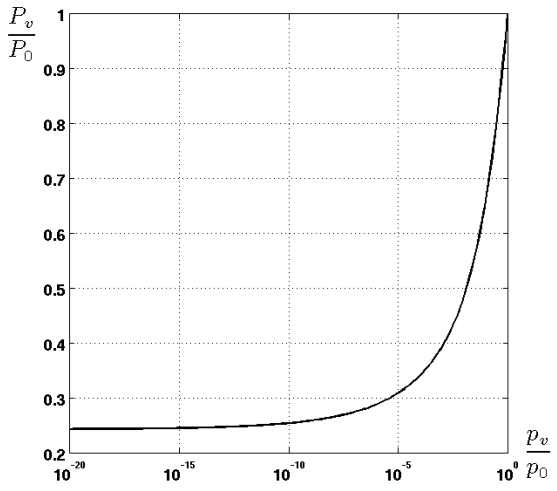

Figure 3-5: Momentum of the incident blast wave just before reflection as a function of the buffer pressure, $l_v = L = 1\text{m}$, $p_s = 8.7$ bar.

pressure. This near zero buffer pressure is the 'threshold buffer pressure'. Equation (3.76e) simplifies greatly when p_v is lower than the threshold buffer pressure.

$$\text{When } p_v \to 0, (1 + k_1k_2)\sqrt{k_4(R-1)+1} \to k_1k_3(R-1), \tag{3.77a}$$

$$\text{or approximately, } (1 + k_1k_2)\sqrt{k_4(R-1)+1} = k_1k_3(R-1), \tag{3.77b}$$

$$(1 + k_1k_2)^2(k_4(R-1)+1) = (k_1k_3)^2(R-1)^2. \tag{3.77c}$$

Solving the quadratic equation (3.77c)(R is always ≥ 1) gives

$$R = 1 + \frac{1}{k_4}\frac{\kappa^2 + \sqrt{\kappa^4 + 4\kappa^2}}{2}, \kappa = \frac{k_4 + k_1k_2k_4}{k_1k_3}, \tag{3.78a}$$

$$\frac{P_v}{P_0} = \frac{\gamma_2\bar{u_s} + \sqrt{2\gamma_2^2\bar{u}_s^2 + 32}}{4\sqrt{1 + \frac{\kappa^2+\sqrt{\kappa^4+4\kappa^2}}{2}\left(1 - \frac{p_0}{p_s+\rho_s u_s^2}\right)}}, \text{ (From equation (3.75b))}, \tag{3.78b}$$

Equation (3.78b) gives a simplified expression for the maximum reduction in the incident wave momentum (note that $l_v = L$) that can be obtained for a shock wave of a given strength. The concept of the threshold pressure can be explained through equation (3.78b) also. When $Rp_v/p_s \to 0$, it is observed that this equation has no term containing p_v. This implies that as long as the strength of the smaller shock is

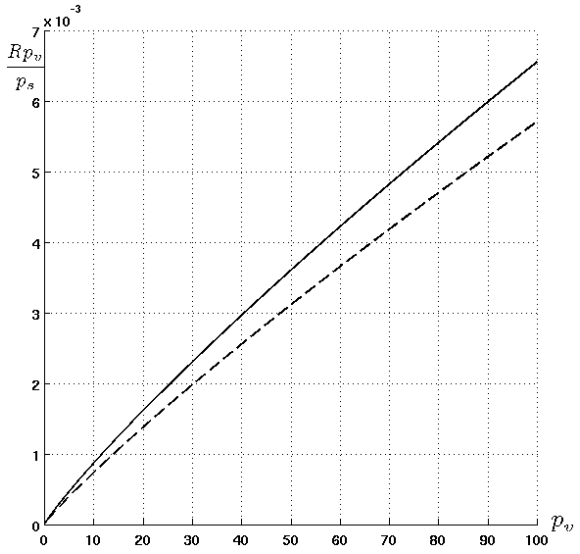

Figure 3-6: Variation of p_1/p_s with p_v in atm. The black solid line denotes p_s=1e5 pa and the black dotted line denotes p_s=3e7 Pa.

small compared to the main shock, the mitigation remains constant. The maximum reduction predicted through equation (3.78b) is verified with the maximum reduction obtained exactly through equation (3.75b) in Table 3.2. The comparison shows that the prediction is accurate compared to the exact results.

Table 3.2: Maximum impulse reduction obtained for given shock strength and buffer length through exact and simplified expressions, l_v = L = 1m.

Shock strength		P_v/P_0	
u_s in ms^{-1}	p_s in bar	Exact	Limit
150	1.7123	0.3497	0.3497
200	2.0259	0.2936	0.2936
500	4.8979	0.2356	0.2355
750	8.7	0.2425	0.2425
1000	14.071	0.2507	0.2507

3.6 Variation of the Shock Strength

The relative momentum, P_{rv} is plotted as a function of the shock strength, p_s/p_0 in Figure 3-7, for l_v = 0.3m, L = 1m and p_v = 0.001 atm. P_{rv} decreases with increasing shock strength and then remains approximately constant. This implies

that the effectiveness of the buffer in mitigating blast impulse reduces as the shock strength increases.

3.7 Approximate Analytical Solution for the Incident Wave Momentum

Equation (3.60) is evaluated using the bisection method. The use of an iterative method can be eliminated altogether by reducing the order of the equation using an approximation. The Taylor's series is used to expand the term $R^{1/7}$ to a first order accuracy around R = 1. The equation for R then simplifies to a polynomial equation of third order and the solutions can be obtained in a closed form without any iterations. Using Taylor's series for an approximation of $(Rp_v/p_s)^{1/7}$ around R = 1 or $Rp_v/p_s = p_v/p_s$,

$$\left(\frac{Rp_v}{p_s}\right)^{\frac{1}{7}} = \left(\frac{p_v}{p_s}\right)^{\frac{1}{7}} + \left(\frac{1}{7}\right)\left(\frac{p_v}{p_s}\right)^{-\frac{6}{7}}\left(\frac{Rp_v}{p_s} - \frac{p_v}{p_s}\right) + O\left(\left(\frac{Rp_v}{p_s} - \frac{p_v}{p_s}\right)^2\right), \quad (3.79a)$$

$$\left(\frac{Rp_v}{p_s}\right)^{\frac{1}{7}} = \left(\frac{p_v}{p_s}\right)^{\frac{1}{7}} \frac{R+6}{7}. \quad (3.79b)$$

Combining equation (3.79b) and equation (3.75b)

$$\begin{aligned} & AR^3 + BR^2 + CR + D = 0, \\ \text{where} \quad & A = k_4\chi_4^2, \\ & B = \chi_2^2\chi_4^2 - 2\chi_4\chi_6k_4 - \chi_3^2, \\ & C = \chi_6^2k_4 - 2\chi_2\chi_4\chi_6 + 2\chi_3^2, \\ & D = \chi_2\chi_6^2 - \chi_3^2, \\ & \chi_1 = 1 + k_1k_2, \quad \chi_2 = 1 - k_4, \quad \chi_3 = k_1k_3, \\ & \chi_4 = \frac{1}{7}\left(\frac{p_v}{p_s}\right)^{\frac{1}{7}}, \quad \chi_5 = 6\chi_4, \quad \chi_6 = \chi_1 - \chi_5. \end{aligned} \quad (3.80)$$

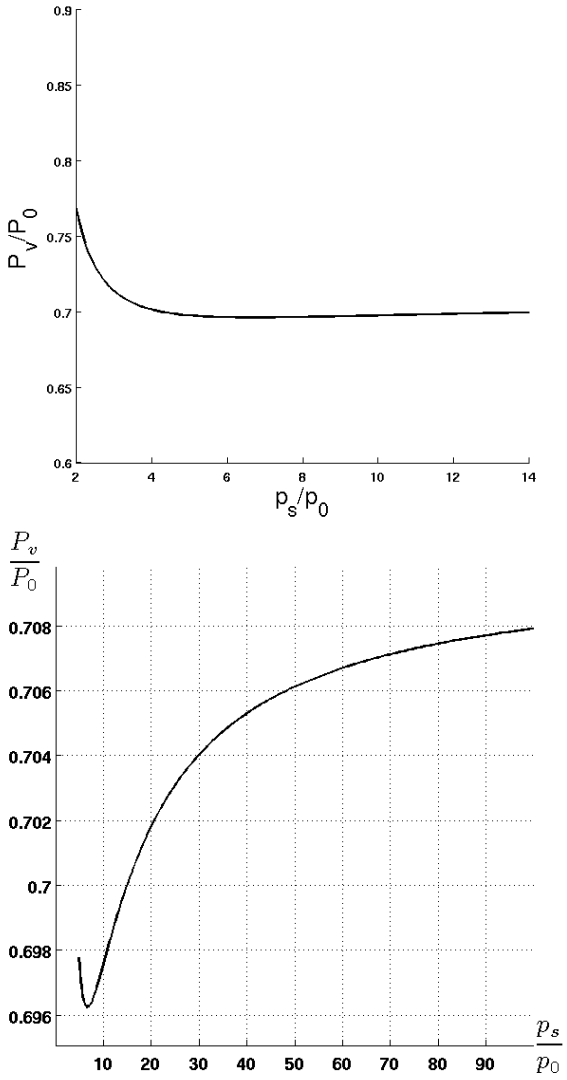

Figure 3-7: Momentum of blast wave just before reflection as a function of p_s for strong shocks, $p_v = 0.001$ atm, $l_v/L = 0.3$.

The solution for equation 3.80 can be obtained analytically and it reads as

$$R = -\frac{B}{3A} - \frac{2^{\frac{1}{3}}(-B^2 + 3AC)}{\alpha\beta} + \frac{\alpha}{2^{\frac{1}{3}}\beta},$$
$$\beta = 3A,$$
$$\alpha = \left(-2B^3 + 9ABC - 27A^2D + \sqrt{4(-B^2 + 3AC)^3 + (-2B^3 + 9ABC - 27A^2D)^2}\right)^{\frac{1}{3}} \tag{3.81}$$

Once R is obtained through equation (3.81), P_v/P_0 can be calculated in a straightforward manner from equation (3.75b). A comparison of Rp_v/p_s and P_v/P_0 obtained using the exact and the approximate methods as a function of p_v/p_s is made in Figure 3.7. The approximation match well with the exact solutions when the buffer pressure is close to the atmospheric pressure or low compared to atmospheric pressure. In both these cases, the pressure of the smaller shock wave is almost equal to the buffer pressure, or R = 1 and the Taylor series approximation is exact.

3.8 Consistency of the Analytical and the Numerical Results

The validity of the analytical solution derived in equation 3.75b is checked by comparing the momentum reduction obtained using this equation with the momentum reduction obtained through simulations in AMROC. The comparison is shown in Figure 3-9. Both results match very well and there is less than 1% difference in the results obtained from the analytical and the numerical methods.

3.9 Momentum Mitigation in a Uniform Wave and a Point Source Blast Wave

A qualitative comparison is made in Table 3.3 between the momentum reductions in the uniform wave and the point source wave after their interactions with the buffer.

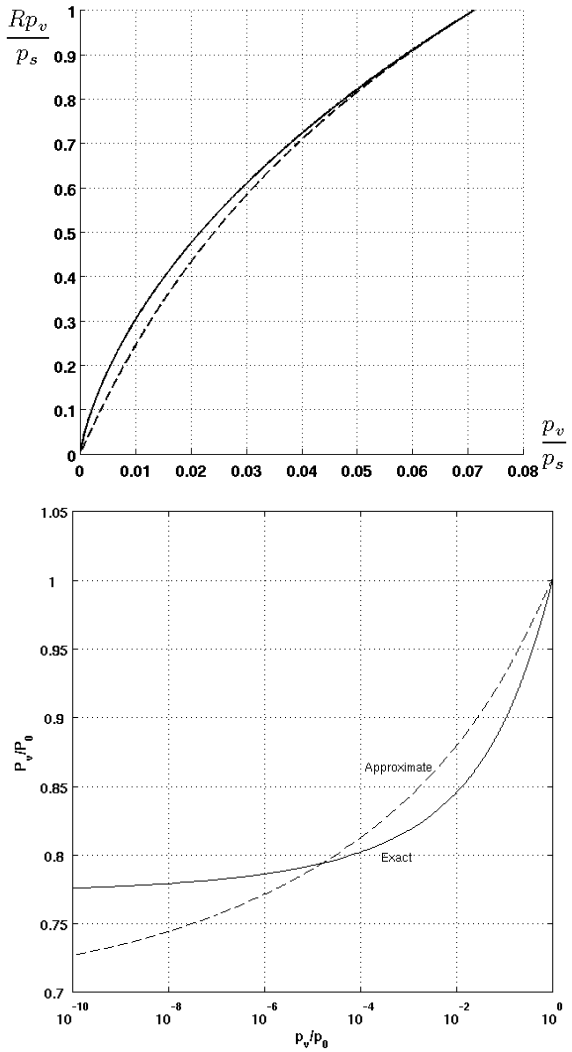

Figure 3-8: Exact (solid) and approximate (dotted) solutions to Rp_v/p_s and P_v/P_0 as a function of p_v/p_s keeping p_s unchanged.

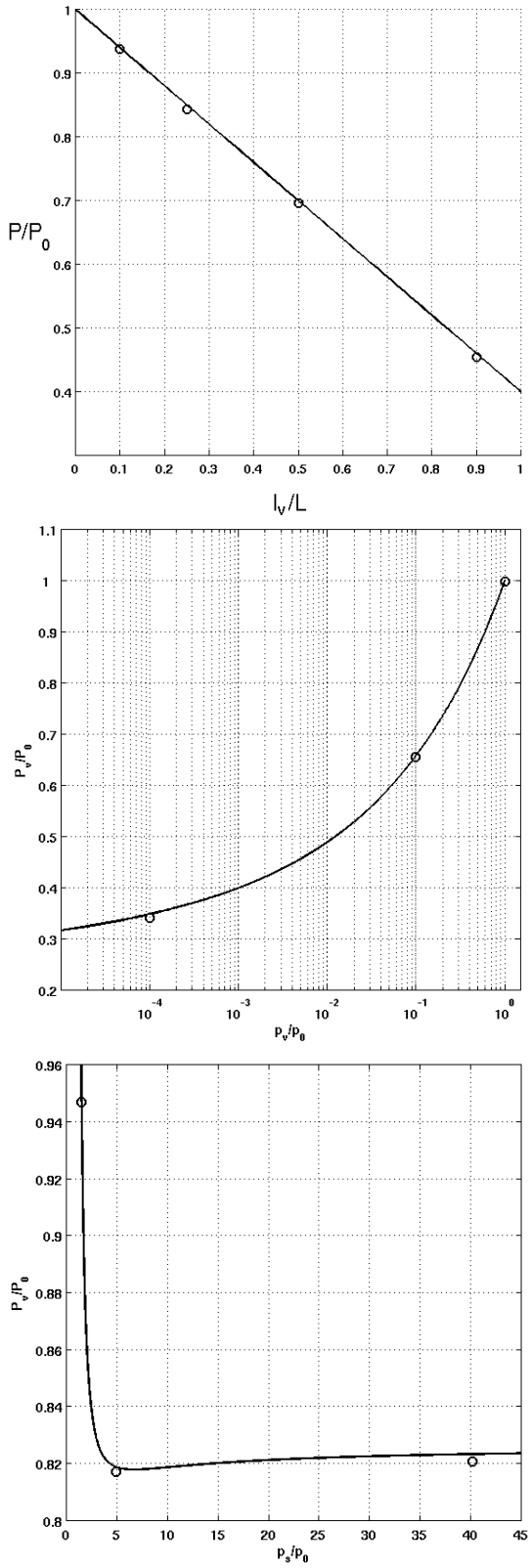

Figure 3-9: Comparison of the momentum reduction obtained from analytical and numerical methods.

Table 3.3: Similarities in the pressure and impulse relief obtained in the uniform wave and the point source blast wave using an air-depleted buffer.

Uniform wave	Point source blast wave
1. The wave structure obtained from the blast-buffer interaction is self similar. The structure consists of a rarefaction wave, a contact discontinuity and a low intensity shock wave. For very low buffer pressures, the rarefaction wave propagates backwards.	1. The wave structure obtained from the blast-buffer interaction is non self-similar. The structure consists of consists of an unsteady rarefaction wave, a contact discontinuity and a shock wave. For very low buffer pressure, the rarefaction wave propagates backwards.
2. As the buffer pressure decreases, a higher mitigation is seen in the incident momentum. When the buffer pressure is very small, a limit on the mitigation is observed.	2. As the buffer pressure decreases, a higher mitigation is seen in the reflected pressure and the transmitted impulse. When the buffer pressure is very small, a limit on the mitigation is observed.
3. The incident momentum decreases linearly with an increase in the buffer pressure.	3. When the buffer length increases, the reflected pressure and the transmitted impulse decrease monotonically.
4. The mitigation of the incident momentum becomes constant when the shock pressure exceeds a certain value.	4. The mitigation of the reflected pressure becomes constant and the impulse mitigation reaches a no-buffer limit when the blast energy exceeds a certain value.

Chapter 4

Conclusions

The pressure of the blast waves traveling in a medium of depressed air, with pressure and density lower than ambient air, can be significantly lower than the pressure of blast waves traveling in air, depending on the depressed air pressure. Based on this observation, a concept has been proposed that could lead to the development of strategies for blast mitigation. A buffer containing depressed air is placed prior to the target object so that the blast wave interacts with the buffer before impinging on the target.

Simulations have been conducted to examine the role of the buffer in blast mitigation. It has been observed that the interaction of the high intensity blast wave with the low pressure buffer results in an unsteady flow containing a shock wave with a much lower intensity, a contact discontinuity and a rarefaction wave. When the buffer to shock pressure ratio is extremely low, the original blast wave is totally defeated and is replaced by a rarefaction wave traveling backwards. Non-dimensional parameters that govern the problem have been derived to characterize the effect of the input parameters on the impact of the blast wave on the structure. The reductions in the maximum reflected pressure and the maximum impulse on the wall in the presence of buffer have been analyzed with changes in the buffer length, buffer pressure and the energy of the blast source. The lower the buffer pressure and higher the buffer length, the more significant is the overpressure and impulse relief.

The pressure and impulse mitigation remains unchanged when the buffer pressure

is reduced below a threshold pressure. This threshold pressure decreases with an increase in buffer length and remains almost the same for incident overpressures varying from a few tenths of an atmosphere to a few atmospheres. The buffer layer is effective for impulse relief for incident overpressures in this range. This makes the concept very relevant for design of protection systems for injury mitigation.

By approximating the blast wave as a uniform shock wave, an analytical solution for the wave structure resulting from the blast-buffer interactions has been presented. An expression for the reduction in the incident wave momentum in the presence of the buffer has been derived. A good match has been obtained between the analytical results and numerical results obtained from simulations of uniform shock interaction with the buffer. The reduction in the incident wave momentum in the presence of a buffer increases linearly with buffer length and remains almost the same when the buffer pressure is reduced below a threshold pressure.

The concept of air-vacated buffer layers could be used in the development of strategies to reduce the damaging effects of blast waves on structures, vehicles and people. The concept could be applied to develop blast protection systems such as air-vacated sandwich panels, helmets with a depressed-air core etc.

The author proposes extension of the work presented in this thesis in the following directions:

1) Modeling of blast-buffer interaction and consequent reflection from a plate of finite mass to understand the combined effects of Fluid Structure Interaction and the airvacation strategies.

2) Investigation of pressure and impulse histories on a plate in a two or three dimensional geometry after blast-buffer interaction to include the role of diffraction in pressure relief.

3) Extension of the analytical solutions from the uniform shock wave interaction with the buffer to simple wave and unsteady shock wave interaction with the buffer.

4) Modeling of the geometry of air-vacated sandwich panels and numerical experiments on their potential benefits for overpressure and impulse relief of blast waves.

5) Investigation of pressure and impulse histories on a wall when the sound speed in the buffer is not necessarily equal to the sound speed in air in general. Investigation of the influence of the buffer pressure and buffer density individually on the overpressure relief in particular.

This thesis has not addressed the practical issues in the implementation of the air-vacated buffer concept. Some of them include detailing a procedure to deplete the air layer near the target structure and maintaining equilibrium at the wall with depressed air on one side and ambient air on another. It is hoped that future work will be able address these issues which would help further the work done so far towards the design and implementation of protection systems utilizing the proposed concept for blast mitigation.

Bibliography

[1] The National Counterterrorism Center Counterterrorism Calender 2009. 4 April 2009. http://www.nctc.gov/site/calendar/index.html.

[2] J. D. Anderson. *Modern Compressible Flow: With Historical Perspective*. McGraw-Hill, New York, 2003.

[3] M. F. Ashby, A. Evans, N. A. Fleck, L. J. Gibson, J. W. Hutchinson, and H. N. G. Wadley. *Metal Foams*. Butterworth Heinemann, 2000.

[4] S. K. Aslanov. On the theory of blast waves. *Combustion, Explosion, and Shock Waves*, 42:450–455, 2006.

[5] W. E. Baker. *Explosion In Air*. University of Texas Press, Texas, 1973.

[6] W. E. Baker, P. A. Cox, P. S. Westine, J. J. Kulesz, and R. A Strehlow. *Explosion Hazards and evaluation*. Elsevier, Amsterdam, 1983.

[7] M. Berger and J. Oliger. Adaptive mesh refinement for hyperbolic partial differential equations. *Journal of Computational Physics*, 53:484–512, 1984.

[8] D. Bogosian, J. Ferritto, and Y. Shi. Measuring uncertainty andh conservatism in simplified blast models. *Presented at the 30th Explosives Safety Seminar, Atlanta, Georgia*, August 2002.

[9] I. Bowen, E. Fletcher, D. Richmond, F. Hirsch, and C. White. Biophysical mechanisms and scaling procedures applicable in assessing responses of the thorax energized by air-blast overpressures or by non-penetrating missiles. *Ann N Y Acad Sci*, 152:122–146, 1968.

[10] H.L. Brode. Numerical solution of spherical blast waves. *Journal of Applied Physics*, 26(6):766–775, 1955.

[11] T. Bui. Computation of point explosion taking into account counter-pressure. 2007.

[12] Edited by G.C. Mays and P.D. Smith. *Blast effects on buildings : design of buildings to optimize resistance to blast loading*. American Society of Civil Engineers, New York, 1995.

[13] J. Caltagirone, M. Dode, and D. Kossover. Structures to Resist the Effects of Accidental Explosions (TM 5-1300, NAVFAC P-397, AFM 88-22). Revision of Tri-Service Regulatory Design Manual. Report 466, Defense Technical Information Center, 1990.

[14] S. Chandrasekhar. On the decay of plane shock waves. Technical Report BRLR 423, Ballistic Research Laboratories, 1943.

[15] J. K. Clutter, J. T. Mathis, and M. W. Stahl. Modeling environmental effects in the simulation of explosion events. *International Journal of Impact Engineering*, 34:973–989, May 2007.

[16] P. W. Cooper. *Explosives Engineering*. Wiley-VCH, New York, 1970.

[17] National Research Council. Protecting buildings from bomb damage. Technical report, National Academy Press, 1995.

[18] R. Courant and K.O. Friedrichs. *Supersonic Flow and Shock Waves*. Springer, New York, 1999.

[19] J. Cummings, M. Aivazis, R. Samtaney, R. Radovitzky, S. Mauch, and D. Meiron. A virtual test facility for the simulation of dynamic response in materials. *J. Supercomput.*, 23:39–50, 2002.

[20] R. Deiterding. A generic framework for blockstructured adaptive mesh refinement in object-oriented C++. http://amroc.sourceforge.net/.

[21] R. Deiterding, R. Radovitzky, S. Mauch, L. Noels, J. Cummings, and D. Meiron. A virtual test facility for the efficient simulation of solid material response under strong shock and detonation wave loading. *Engineering with Computers*, 22(3-4):325–347, 2006.

[22] V.S. Deshpande and N.A. Fleck. One-dimensional response of sandwich plates to underwater shock loading. *Journal of the Mechanics and Physics of Solids*, 53:2347–2383, 2005.

[23] TNT Equivalents for Various Explosives and Fuel-Air Mixtures. 2 January 2009. http://www.nctc.gov/site/technical/tnt.html.

[24] K. O. Friedrichs. Formation and decay of shock waves. *Communications on Pure and Applied Mathematics*, 1:211–245, 12 Oct 1948.

[25] H. P. Greenspan and D. S. Butler. On the expansion of a gas into vacuum. *Journal of Fluid Mechanics*, 13:101–119, 1961.

[26] J.W. Hutchinson and Z. Xue. Metal sandwich plates optimized for pressure impulses. *International Journal of Mechanical Sciences*, 47:545–569, 2005.

[27] N. Kambouchev. *Analysis of Blast Mitigation Strategies Exploiting Fluid-Structure Interaction*. PhD thesis, Department of Aeronautics and Astronautics, MIT, 2007.

[28] N. Kambouchev, L. Noels, and R. Radovitzky. Non-linear compressibility effects in fluid-structure interactions and their implications on the air-blast loading of structures. *Journal of Applied Physics*, 100:063519–1–063519–11, 2006.

[29] K. Kato, T. Aoki, S. Kubota, and M. Yoshida. A numerical scheme for strong blast wave driven by explosion. *International Journal of Impact Engineering*, 51:1335–1353, January 2006.

[30] V. P. Korobeinikov. *Problems of Point Blast Theory*. Americian Institute of Physics, New York, 1991.

[31] C. B. Laney. *Computational Gasdynamics*. Cambridge University Press, New York, 1998.

[32] R. Latter. Similarity solution for a spherical shock wave. *Journal of Applied Physics*, 26(8):954–960, 1955.

[33] S. M. Liang, J. S. Wang, and H. Chen. Numerical study of spherical blast-wave propagation and reflection. *Shock Waves*, 12:59–68, 2002.

[34] Y. Liang, A.V. Spuskanyuk, S.E. Flores, D.R. Hayhurst, J.W. Hutchinson, R.M. McMeeking, and A.G. Evans. The response of metallic sandwich panels to water blast. *Journal of Applied Mechanics*, 74:81–99, January 2007.

[35] H.W. Liepmann and A. Roshko. *Elements of Gasdynamics*. Dover Publications, Inc, New York, 2001.

[36] D. F. Moore, A. Jerusalem, M. Nyein, L. Noels, M. S. Jaffee, and R. Radovitzky. Computational biology - modeling of primary blast effects on the central nervous system. *NeuroImage*. Accepted, 2009.

[37] T. Mukai, H. Kanahashi, T. Miyoshi, M. Mabuchi, T. G. Nieh, and K. Higashi. Experimental study of energy absorption in a close-celled aluminum foam under dynamic loading. *Scripta Materialia*, 40(8):921–927, 1999.

[38] L. Noels, K. Dharmasena, H.N.G. Wadley, and R. Radovitzky. Air shock loading of metallic plates: Experiments and coupled simulations. *International Journal of Solids and Structures*. Submitted, 2007.

[39] D.E. Okhotsimskii, I.A. Kondrasheva, Z.P. Vlasova, and R.K. Kozakova. Calculation of a point explosion taking into account counter pressure. *Tr. Mat. Inst. Steklova*, 50:1–65, 1957.

[40] L. I. Sedov. Propagation of strong shock waves. *Journal of Applied Mathematics and Mechanics*, 10:241–250, 1946.

[41] L. I. Sedov. *Similarity and Dimensional Methods in Mechanics*. CRC Press Inc., Florida, 1993.

[42] G. I. Taylor. The formation of a blast wave by a very intense explosion, II the atomic explosion of 1945. *Proceeding of Royal Society, Series A*, 201(1065):175–186, 1950.

[43] G. I. Taylor. The pressure and impulse of submarine explosion waves on plates, paper written for the civil defence research committee, ministry of home security (1941). In G.K. Batchelor, editor, *The scientific papers of Sir Geoffrey Ingram Taylor*, volume III Aerodynamics and the Mechanics of Projectiles and Explosions, pages 287–303. Cambridge University Press, 1963.

[44] G.I. Taylor. The formation of a blast wave by a very intense explosion, I theorical discussion. *Proceeding of Royal Society, Series A*, 201(1065):159–174, 1950.

[45] J.W. Tringe, J.D. Molitoris, and R.G. Garza et al. Detailed comparison of blast effects in air and vacuum. UCRL-CONF 233223, American Physical Society, August 2007.

[46] A. Vaziri, Z. Xue, and J. W. Hutchinson. Metal sandwich plates subject to intense air shocks. *International Journal of Solids and Structures*, 44:2021–2035, 2007.

[47] D. Venable, R. W. Taylor, and B. T. Rogers et al. United States Patent 3804017, 1974.

[48] The Virtual Test Facility. 2 May 2009. http://www.cacr.caltech.edu/asc/wiki/bin/view/.

[49] J. von Neumann. The point source solution. In A. J. Taub, editor, *John von Neumann: Collected Works*, volume 6, pages 219–237. Permagon Press, 1963.

[50] Von Neumann, J. and Richtmyer, R. D. A method for the numerical calculation of hydrodynamic shocks. *Journal of Applied Physics*, 21:232–237, 1950.

[51] H. N. G. Wadley, K. P. Dharmasena, M. Y. He, R. M. McMeeking, A. G. Evans, T. Bui-Tanh, and R. Radovitzky. An active concept for limiting injuries caused by air blasts. *International Journal of Impact Engineering*. Submitted.